AD-A242 491

212800-4-F

Final Report

SSM/I SEA ICE PRODUCTS VALIDATION

R. JENTZ
C. WACKERMAN
R. SHUCHMAN
Center for Earth Sciences
Advanced Concepts Division

JUNE 1991

Office of Naval Research
800 N. Quincy Street
Arlington, VA 22217
Contract No. N00014-88-C-0680

Approved for public release
Distribution Unlimited

91-14584

ERIM · P.O. Box 134001
Ann Arbor, MI 48113-4001

UNCLASSIFIED
SECURITY CLASSIFICATION OF THIS PAGE

REPORT DOCUMENTATION PAGE

Form Approved
OMB No. 0704-0188

1a REPORT SECURITY CLASSIFICATION UNCLASSIFIED	1b RESTRICTIVE MARKINGS
2a SECURITY CLASSIFICATION AUTHORITY	3 DISTRIBUTION/AVAILABILITY OF REPORT UNLIMITED
2b DECLASSIFICATION/DOWNGRADING SCHEDULE	
4 PERFORMING ORGANIZATION REPORT NUMBERS(S) 212800-4-F	5 MONITORING ORGANIZATION REPORT NUMBER(S)
6a NAME OF PERFORMING ORGANIZATION Environmental Research Institute of Michigan 6b OFFICE SYMBOL (if applicable)	7a NAME OF MONITORING ORGANIZATION Office of Naval Research
6c ADDRESS (City, State, and ZIP Code) 1975 Green Road Ann Arbor, MI 48105	7b ADDRESS (City, State, and ZIP Code) 800 N. Quincy Street Arlington, VA 22217
8a NAME OF FUNDING /SPONSORING ORGANIZATION Office of Naval Research 8b OFFICE SYMBOL (if applicable)	9 PROCUREMENT INSTRUMENT IDENTIFICATION NUMBER N00014-88-C-0680
8c ADDRESS (City, State, and ZIP Code) 800 N. Quincy Street Arlington, VA 22217	10 SOURCE OF FUNDING NUMBERS PROGRAM ELEMENT NO / PROJECT NO / TASK NO / WORK UNIT ACCESSION NO

11 TITLE (Include Security Classification)
SSM/I Sea Ice Products Validation

12 PERSONAL AUTHOR(S)
R.R. Jentz, C.C. Wackerman

13a TYPE OF REPORT	13b TIME COVERED	14 DATE OF REPORT (Year, Month, Day)	15 PAGE COUNT
Technical	FROM 7/88 TO 9/90	June 1991	86

16 SUPPLEMENTARY NOTATION

17 COSATI CODES			18 SUBJECT TERMS (Continue on reverse if necessary and identify by block number)
FIELD	GROUP	SUB-GROUP	

19 ABSTRACT (Continue on reverse if necessary and identify by block number)

The Special Sensor Microwave/Imager (SSM/I), which is part of the Defense Meteorological Satellite Program (DMSP), is a coarse resolution passive microwave sensor with good aerial coverage of the Arctic region. Since the SSM/I sensor produces nearly full coverage of the Arctic region each day, data gathered by this sensor is used to obtain geophysical parameters assoicated with the Arctic area. An algorithm has been developed at Goddard Space Flight Center which produces both multiyear and total ice concentration estimates from SSM/I data. This paper will present comparisons between these SSM/I derived ice concentration estimates and estimates derived from high resolution SAR data that was collected co-incident to the SSM/I overpass. Data from the Beaufort and Bering Seas collected in March of 1988 is used and both the multiyear concentration algorithm and the total ice concentration algorithm are compared. A discrepancy between the two estimates is analyzed and a possible explanation based on the scattering from ridging in first-year ice is presented.

20 DISTRIBUTION/AVAILABILITY OF ABSTRACT XX UNCLASSIFIED/UNLIMITED ☐ SAME AS RPT ☐ DTIC USERS	21 ABSTRACT SECURITY CLASSIFICATION UNCLASSIFIED
22a NAME OF RESPONSIBLE INDIVIDUAL Robert Jentz	22b TELEPHONE (Include Area Code) 313 994-1200 22c OFFICE SYMBOL

DD Form 1473, JUN 86
ERIM 116

Previous editions are obsolete.

UNCLASSIFIED
SECURITY CLASSIFICATION OF THIS PAGE

CONTENTS

LIST OF FIGURES v
LIST OF TABLES vi
1.0 INTRODUCTION 1
2.0 EXECUTIVE SUMMARY 3
3.0 SSM/I-SAR SEA ICE CONCENTRATION COMPARISON 5
3.1 SENSOR AND DATA SET DESCRIPTION 6
3.2 IMAGE DATA ANALYSIS 14
3.3 RESULTS OF COMPARISON 26
3.4 DISCUSSION 36
4.0 SAR SEA ICE SEGMENTATION ALGORITHMS 46
4.1 COARSE RESOLUTION SEA ICE CLASSIFICATION ALGORITHM 46
4.2 HIGH-RESOLUTION SEA ICE CLASSIFICATION ALGORITHM 51
4.2.1 Optimal Algorithm 60
4.2.2 Data Results 59
4.2.3 Summary and Conclusions 69
5.0 CONCLUSIONS 70
6.0 REFERENCES 71
APPENDIX. 73

Accession For
NTIS GRA&I
DTIC TAB
Unannounced
Justification
By
Distribution/
Availability Codes
Dist | Avail and/or Special
A-1

LIST OF FIGURES

3-1. March 1988 Alaska Collection Locations 10

3-2. P-3 SAR Double Swath, Low Resolution Mode Used During the March 1988 Alaska Data Collection 12

3-3. Photographic Mosaic of Digital SAR Data Collected in the Beaufort Sea on 18 March 1988 15

3-4. Photographic Mosaic of Digital SAR Data Collected in the Beaufort Sea on 19 March 1988 19

3-5. Photographic Mosaic of Digital SAR Data Collected in the Bering Sea on 21 March 1988 21

3-6. March 18, 1988 Multiyear Ice Concentration Estimates Plotted for Both the SAR and SSM/I Data Along with the Linear Trend 28

3-7. March 19, 1988 Multiyear Ice Concentration Estimates Plotted for Both the SAR and SSM/I Data Along with the Linear Trend 29

3-8. Multiyear Ice Concentration Error With Linear Trend Plotted for 18 March 1988 Alaska Data 32

3-9. Multiyear Ice Concentration Error With Linear Trend Plotted for 19 March 1988 Alaska Data 33

3-10. March 21, 1988 Total Ice Concentration Estimates Plotted for Both SAR and SSM/I Data Along with the Linear Trend 37

3-11. Total Ice Concentration Error With Linear Trend Plotted for 21 March 1988 Alaska Data 39

4-1. Coarse Resolution (approx. 100 m Grid) SAR Image Corresponding to Area 8 of the March 18, 1988 Photographic Mosaic Shown in Figure 3-3 49

4-2. Histogram of the Coarse Resolution SAR Image Given in Figure 4-1 52

4-3. Binary Map of Coarse Resolution SAR Data Thresholded at 790 53

4-4. Binary Map of Coarse Resolution SAR Image After a Nearest Neighbor Operation was Performed to Remove Isolated Pixels 55

4-5. Optimal Combination of Ratios of Statistics Measures for MIZEX Data 62

4-6. Optimal Combination of Ratios of Texture Measures for MIZEX Data 63

LIST OF FIGURES (cont.)

4-7. Optimal Combination of Ratios of Statistics Measures for Only Three Classes of MIZEX Data 64

4-8. Optimal Combination of Ratios of Texture Measures for Only Three Classes of MIZEX Data 65

4-9. Optimal Combination of Ratios of Statistics Measures for Alaska Data 67

4-10. Optimal Combination of Ratios of Texture Measures for Alaska Data 67

LIST OF TABLES

3-1. P-3 SAR Operating Parameters 9

3-2. March 1988 SAR Alaska Collection Flight Times 11

3-3. Global Tie-Points for the NASA SSM/I Sea Ice Algorithm 25

3-4. SAR-SSM/I Multi Year Ice Concentration Estimates Derived From 50 km Areas of Data Gathered During the March 1988 Alaska Survey 27

3-5. Linear Regression Parameters for the Plots in Figures 3-6 and 3-7 30

3-6. Linear Regression Parameters for the Plots in Figures 3-8 and 3-9 34

3-7. March 21, 1988, Lat. 57.10° - 59.90°, Long. 191.40° - 193.45° 35

3-8. Linear Regression Parameters for the Plots in Figures 3-10 and 3-11 38

3-9. Results of Pressure Ridge Analysis 44

4-1. Optimal Clustering Metric for Each Measurement Vector and Data Set 68

1.0 INTRODUCTION

Throughout the next two decades large amounts of both active and passive microwave imagery collected over the polar region will be available to the polar research community. The passive microwave data will be provided by the Special Sensor Microwave/Imager (SSM/I) which is the first of seven planned SSM/I's scheduled for launch over the next two decades each with a life expectancy of approximately three years [1]. The current SSM/I sensor has been producing passive microwave data of the arctic region since its launch, providing the polar scientific community with nearly full global coverage every day. This allows for the continued research of polar sea ice observations which began in 1972 with the Nimbus 5 Electrically Scanning Microwave Radiometer (ESMR), and continued to 1987 with the Nimbus 7 Scanning Multichannel Microwave Radiometer (SMMR). The active microwave data will come from various satellite and aircraft mounted Synthetic Aperture Radar (SAR) systems. The majority of the active microwave data will be provided by the SAR Alaska Station which will be able to rapidly produce SAR imagery from EOS, RADARSAT, ERS-1, and possibly a Japanese ERS. The images generated by these systems contain both geophysical and morphological information about the arctic region along with the kinematics of the area. Previous polar research studies have focused on extracting geophysical information regarding ice floe size distributions, open water lead locations, sea ice concentration maps, and sea ice extent (location of the boundary between open water and the ice pack). The daily production of the sea ice concentration maps assist in the navigation of ships both in and around the arctic region along with the generation of global climate models. In addition, having the ability to monitor the motion of ice floes with respect to time will routinely influence decisions regarding location and scheduling of offshore drilling operations, as well as decisions to suspend drilling activities at sites threatened by large ice floes.

The potential of imaging radars for discriminating sea ice types has been demonstrated using manual photographic interpretation techniques [2,3]. These studies show the ability of high-resolution SAR sensors to obtain imagery independent of solar illumination and weather conditions. Also, high-resolution SAR systems are able to delineate between individual ice floes which makes the determination of different sea ice types easier. For these reasons, the polar research community has expended an enormous effort trying to develop automatic or near real-time algorithms for extracting this geophysical information.

The problem of verifying the results generated from algorithms designed to extract this geophysical information is rather difficult. The approach in the past (when ground truth data is not available) has been to compare the results produced from coincident data sets collected by multiple sensors, then try and explain any discrepancies found. The research effort reported in this document adopts this approach. The focus of this analysis is; (1) to use sea ice concentration estimates generated from high-resolution SAR imagery to validate ice concentration estimates produced by the NASA Team sea ice concentration algorithm applied to relatively coarse resolution SSM/I data, and (2) to develop sea ice classification algorithms which are designed to separate different sea ice types for both high-resolution and coarse resolution SAR imagery.

This report is divided into five parts; section 2.0 presents an executive summary, section 3.0 discusses the SAR and SSM/I sea ice concentration comparison performed, section 4.0 presents both a coarse resolution ice classification algorithm designed to separate different ice types from highly multilooked SAR imagery, along with a high-resolution classification algorithm designed to find the optimum linear combination of tonal and textural measures that separate multiple ice types, and finally section 5.0 summarizes the results of this analysis.

2.0 EXECUTIVE SUMMARY

Validation of arctic sea ice parameters generated from SSM/I data began shortly after its launch in June 1987. In March 1988, a series of coordinated SSM/I underflights were performed by the NADC/ERIM SAR in Alaska and its surrounding coastal areas as part of the NASA Defense Meteorological Satellite Program (DMSP) SSM/I Sea Ice Validation Program. Coincident sea ice imagery was collected in the Beaufort Sea on the 18th and 19th, the Bering Strait on the 21st, and the Chukchi Sea on the 22nd. This data is used to determine the accuracy of SSM/I total and multiyear ice concentrations generated by the NASA Team sea ice algorithm.

The SAR sea ice data collected on both the 18th and 19th of March is used to validate the multiyear ice concentration estimates generated from the SSM/I overflights, while the data recorded on the 21st is used to validate the total ice concentration estimates. The SAR concentration estimates are produced manually from a SAR photographic mosaic generated by optically processing the digital SAR data. The SAR mosaics cover an area approximately 100 km by 300 km encompassing approximately ten SSM/I footprints where each of the SSM/I footprints represent a 50 km area. The SAR concentration estimates are derived by separating each of the SSM/I footprints into four hundred 2.5 km areas and manually interpreting concentration estimates for each. The four hundred 2.5 km areas are then averaged to produce a single estimate corresponding to the entire SSM/I footprint. These SAR concentration estimates are then compared to concentration estimates generated by the NASA Team sea ice algorithm (referred to as the SSM/I estimates). A linear regression analysis was performed between the SAR and SSM/I estimates to determine the accuracy of the SSM/I results. The regression analysis showed that the multiyear estimates are similar for the March 19th data (March 19th imagery represents an area well into the multiyear ice pack) while relatively large differences were found in the March 18th data (March

18th imagery crosses the boundary between the first-year and multiyear ice pack). Three possible explanations for these differences are explored including: (1) an alignment error between the coincident SAR and SSM/I pixel locations; (2) the fact that pressure ridges associated with first-year ice in the Beaufort Sea might be misclassified as multiyear sea ice by the Nasa Team algorithm; and (3) the NASA Team sea ice algorithm brightness temperature tie-points are inaccurate for the region over which this comparison takes place.

In addition to the NASA Team ice algorithm validation this project included the development of both coarse and high-resolution SAR ice segmentation algorithms. The coarse resolution algorithm is used to validate the accuracy of the manually derived SAR concentration estimates used in the comparison. This algorithm entails processing the digital SAR data as if it where real aperture radar data (i.e., performing range compression only) and averaging to a 100 km grid spacing. The averaging highly multilooks the data such that any azimuth smearing caused by the quadratic phase term is eliminated. The density function associated with the highly multilooked data is multimodal suggesting threshold values which will separate the data into multiple ice types. The high-resolution algorithm is a method for estimating the optimal linear combination of a given set of image features which give the maximal separation of the resulting classes. The set of image features used in this algorithm include both first order statistics which exploit the tonal information associated with SAR imagery along with six texture measures derived from a general co-occurrency matrix. The texture measures are inertia, cluster shade, cluster prominence, local homogeneity, energy, and entrope.

3.0 SSM/I-SAR SEA ICE CONCENTRATION COMPARISON

Verification of SSM/I ice concentrations is often difficult due to the lack of available ground truth and the need to characterize large areas (i.e., greater than 15 to 25 km square pixels). One solution is to compare SSM/I ice concentration estimates to those derived by other sensors. High-resolution aircraft SAR systems can provide such a verification since the generation of reliable ice concentration estimates can be performed [2,3]. These studies show that the high spatial resolution (approximately 3m square pixels) associated with SAR imagery provides the ability to delineate individual floes and leads which make the determination of ice concentration easier. It has also been shown that sea ice concentration estimates generated from both passive and active microwave sensors over coincident scenes produce similar results using a single channel linear concentration algorithm [2,4]. However, the analysis described here will use sea ice concentration estimates produced from high-resolution SAR imagery (where there are approximately 300 million SAR pixels corresponding to each SSM/I pixel) to validate ice concentration estimates generated specifically from the multichannel SSM/I data. The SAR derived ice concentration estimates are produced by a manual analysis of mosaiced imagery while the SSM/I estimates are generated by a multichannel concentration algorithm which utilizes both the polarization and spectral gradient ratios to determine the percentage of multiyear sea ice [5,6,7].

This chapter is divided into four sections; 3.1 will present a description of both sensors along with a narrative covering the Alaska data collection, section 3.2 discusses the concentration algorithms used along with an analysis pertaining to the accuracy of the SAR concentration estimates, section 3.3 will summarize the results of the comparison, and section 3.4 will discuss possible causes of the differences found in the concentration estimates.

3.1 SENSOR AND DATA SET DESCRIPTION

The SSM/I is a multichannel passive microwave radiometer mounted on the DMSP 5D-2 Spacecraft F8 which was launched on 19 June 1987. It was built by Hughes Aircraft and was designed to provide synoptic maps of atmospheric, oceanographic, and selected land parameters on a global scale. The SSM/I contains seven linearly-polarized channels operating at four separate frequencies (i.e.,, both horizontal and vertical polarization at 19.3, 37.0, and 85.5 GHz and vertical polarization at 22.2 GHz). The SSM/I satellite is in a circular sun-synchronous near-polar orbit at an altitude of approximately 800 km. The orbit period is 102.0 minutes producing 14.1 full orbit revolutions every day. The scanning antenna is tilted at a 45 degree angle to the satellite spin axis and sweeps out a 1400 km wide swath in 1.9 seconds. The resolution, or footprint, of the SSM/I brightness temperature varies according to the frequency where the footprint is approximately 55, 49, 32, and 13 km for the 19.3, 22.2, 37.0, and 85.5 GHz channels respectively. For a complete explanation of the SSM/I system see [8].

The NADC/ERIM SAR (also referred to as the P-3 SAR) is a multifrequency, polarimetric SAR installed in a U.S. Navy P-3 aircraft. It is a side-looking SAR that operates in strip-map mode, and is capable of looking out either side of the aircraft. The center frequencies are 9.35 GHz, 5.30 GHz, and 1.25 GHz corresponding to X, C, and L bands respectively. The system is capable of recording polarimetric data corresponding to all of the elements of the polarization matrix (i.e., HH, VV, HV, and VH polarizations) where transmit and receive polarizations can be altered on a pulse-by-pulse basis. High density digital tape (HDDT) is the primary storage medium for the digital data which is collected from each of the four channels. A block of auxiliary data describing the radar flight path and geometry are also recorded for each pulse and stored with the digital data on HDDT. The data from a single channel, selectable by the users, are also recorded on a real-

time image formation processor along with photographic film which is used for subsequent optical processing.

The P-3 SAR operates in five different swath modes with varying combinations of frequency/polarization. In single-swath-multiplex mode the system collects any four frequency/polarization combinations with each of the four channels containing the same range coverage. The azimuth (along track) data are presumed to a rate one-sixth the no-presume rate and 4096 range bins are recorded per channel. The single-swath-polarimetric mode is similar to the single-swath-multiplex mode with the same range coverage in each of the four channels, hence, the same number of range bins. A single frequency band is used with all four polarization combinations where a constant phase shift of the transmitted FM chirp is maintained between the four polarizations. The azimuth records are presumed to one-third the no-presume rate. The single-swath mode also contains a no-presume mode which records a single frequency band and polarization. The double-swath-multiplex mode records two channels of data with varying combinations of frequency/polarization. The range swath is doubled so the number of range bins recorded is 8192 and the presume rate is one-sixth the no-presume rate. The quadruple-swath-multiplex mode records one channel of data corresponding to a single frequency band and polarization. The range swath is increased by four over the single-swath mode so that 16384 range bins can be recorded and the presume rate remains at one-sixth the no-presume rate.

The P-3 SAR operates in one of two resolution modes for any of the swath modes previously described. The slant range coverage at high-resolution mode is 4915 meters in single-swath, 9830 meters in double-swath, and 19660 meters in quadruple-swath modes with azimuth and range resolution being 2.8 meters and 1.6 meters respectively. At low resolution the slant range coverage is 9830 meters in single-swath, 19660 meters in double-swath, and 39320 meters in quadruple-swath modes with an azimuth resolution of 2.8 meters and a range resolution of 3.2

meters. Table 3-1, and reference [9], give an overview of the P-3 SAR operating parameters.

The SAR imagery used in this analysis (referred to as the Alaska data collection or Alaska survey) consisted of data collections on four separate days in and around the Alaskan mainland. Imagery was collected in the Beaufort Sea on the 18th and 19th of March 1988, in the Bering Sea on the 21st of March 1988, and in the Chukchi Sea on the 22nd of March 1988. The flight track locations of the P-3 SAR for each collection date of the Alaska survey, along with an outline of the Alaska coast and surrounding islands, are shown in Figure 3-1. The SAR data collected on both the 18th and 19th of March cover areas of the Beaufort Sea just off the northern coast of Alaska. These collection dates are well into the ice pack such that the imagery contains a combination of both first-year and multiyear sea ice without any areas of open sea water. For this reason, the data collected on the 18th and 19th March is used for the multiyear ice concentration comparison. The SAR data collected on the 21st of March represents an area containing both first-year sea ice and open water just south of the Nunivak Island, and is used for the total sea ice concentration comparison. The SAR data gathered on the 22nd of March contains two flight passes in the multiyear ice pack along with multiple short passes in varying swath, polarization, and resolution modes which will not be used in this analysis.

The SAR data was collected in double-swath-multiplex mode at low resolution (approximately 3 meters in both range and azimuth). The two frequency and polarization combinations used consisted of X-band at HH-polarization, and C-band at VV-polarization. The aircraft collection times, altitude, and velocity are listed in Table 3-2 for each of the four collection dates. Notice that the aircraft flew at an altitude of 6098 meters with a mean velocity of 288 knots and that data was recorded over approximately a seven hour period for each of the four collection dates. Figure 3-2 illustrates the collection geometry for the double-

Table 3-1.
P-3 SAR Operating Parameters

Specification	Value		
Frequency	X, L, C		
Polarization	VV, HH, VH, HV		
Viewing Direction	Left or Right		
Processing	Real-Time, Optical, Digital		
Swath Width in Range Direction	**Single**	**Double**	**Quad**
Narrow Band (High-Res)	4915 m	9830 m	19660 m
Wide Band (Low-Res)	9830 m	19660 m	39320 m
Resolution	**Azimuth x Range**		
High	2.8 m x 1.6 m		
Low	2.8 m x 3.2 m		
Center Frequency Beamwidth	**Vert. Pol**	**Hori. Pol**	
X-Band	1.7°	1.6°	
C-Band	3.6°	3.45°	
L-Band	8.55°	9.75°	

ALASKA SURVEY

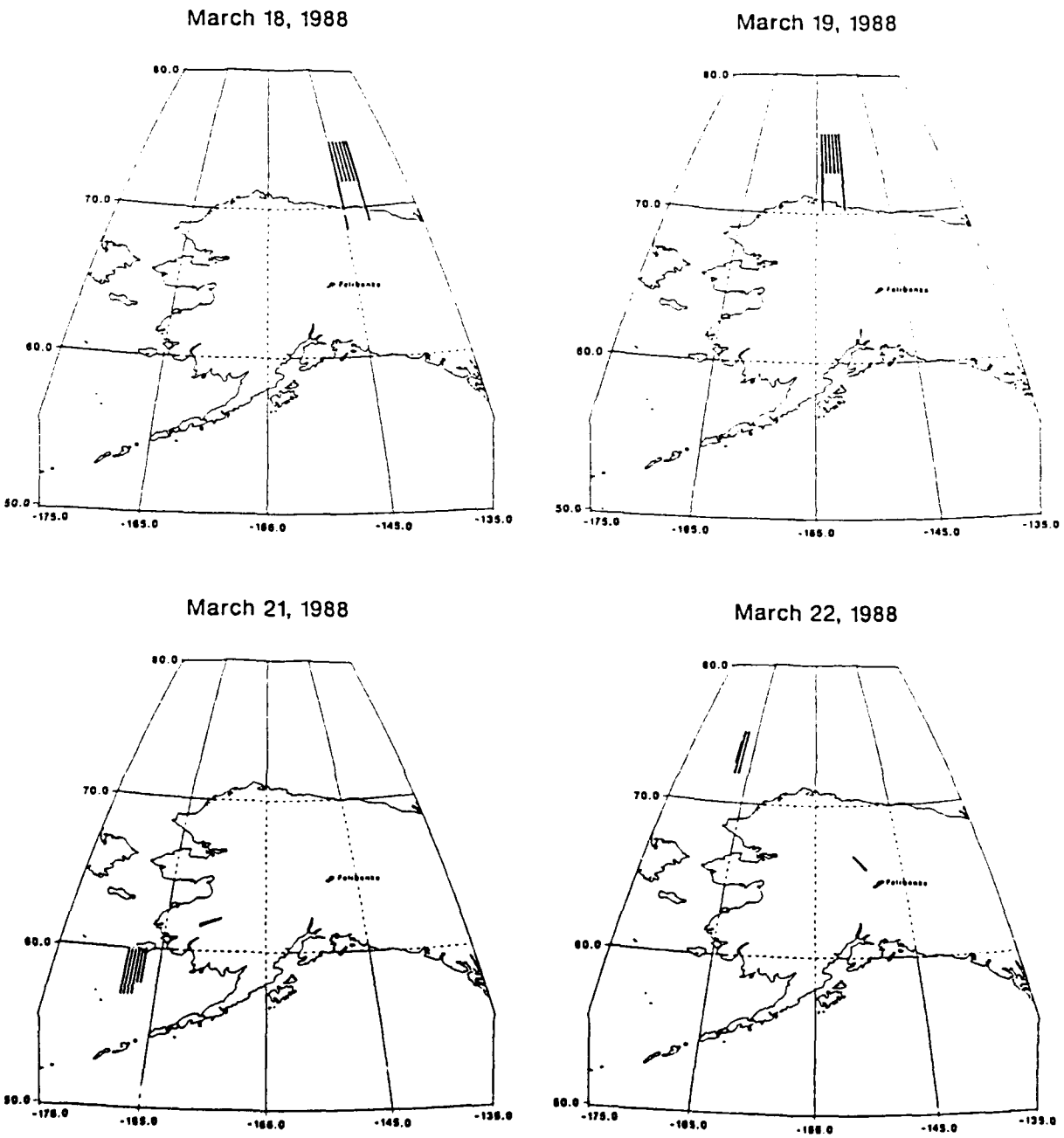

Figure 3-1. March 1988 Alaska Collection Locations

Table 3-2.
March 1988 SAR Alaska Collection Flight Times

Flight Date (Local)	Start Time (UT)	Stop Time (UT)	Altitude (ft)	Average Speed (kts)
18 March 1988	02:35:06	10:16:58	20,000	221
19 March 1988	02:59:57	10:27:52	20,000	287
21 March 1988	03:03:34	09:52:51	20,000	293
22 March 1988	04:17:33	11:06:09	20,000	301

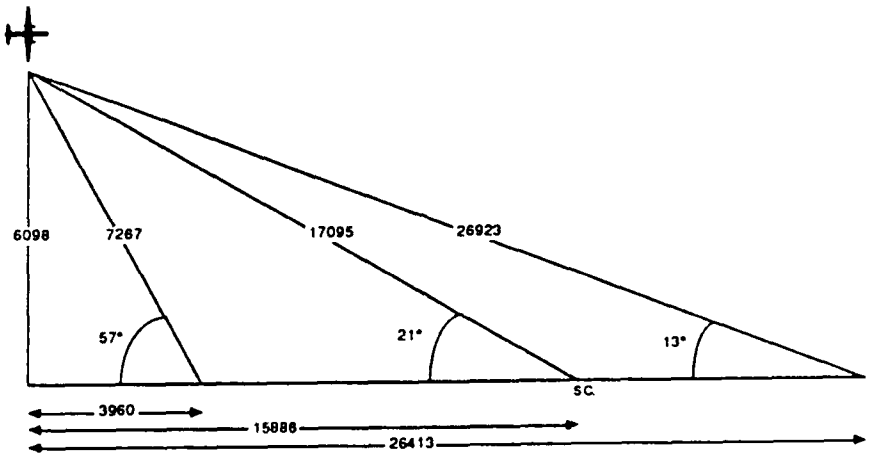

(a) Double Swath, Low Resolution

Figure 3-2. P-3 SAR Double Swath, Low Resolution Mode Used During the March 1988 Alaska Data Collection.

swath, low resolution mode of the P-3 SAR used on all four of the collection dates. The slant range distance to the near edge of the radar swath is 7267 meters which corresponds to an incidence angle of 33°, and the slant range distance to the far edge of the radar swath is 26923 meters corresponding to an incidence angle of 77°. This provides a swath width of 22.270 kilometers of uninterrupted image coverage in the ground plane. The flight lines were planned to provide approximately three kilometers of overlap between adjacent passes. This overlap was more than adequate to ensure continuous data coverage even with the possibility of navigation errors.

The SAR flights were planned to be coincident with the SSM/I overflights in both time and location for each of the four collection dates. The SAR data collected on the 18th, 19th, and 21st of March represent continuous blocks of the ground surface each covering an area approximately 300 kilometers by 100 kilometers in size. Each of the 300 X 100 kilometer blocks of SAR data correspond, in latitude, to approximately six scans of the SSM/I sensor. At 1.9 seconds per SSM/I scan the area represented by each block of SAR imagery corresponds to less than 15 seconds of SSM/I data. Since the SAR data was collected over a seven hour period and the SSM/I satellite only takes 102 minutes to complete one revolution of its orbit, the SAR and SSM/I data is coincident in time to within a five hour period. The stability of the Beaufort Sea ice implies that very little change in ice conditions would be noticed over this five hour period. Therefore, the multiyear sea ice concentration comparison performed on the Beaufort Sea data collected on the 18th and 19th of March should correspond very nicely with the SSM/I data. Even though the SAR data collected in the Bering Sea on the 21st of March represents an area that is more dynamic than the Beaufort Sea, little change would be expected over the five hour period.

The Global Positioning System (GPS) onboard the P-3 aircraft was not available during this experiment. So the P-3 aircraft locations are only as accurate as the Inertial Navigation System (INS) used onboard

the aircraft, which has a mean drift of approximately 1.0 knot. However, the exact location of the P-3 SAR data can be determined by gathering data across coastal regions. This provides reference points that can be compared to map data for verification. This is, in fact, why on the 18th and 19th of March the sensor was recording imagery across the northern Alaska coastline at both the first and last pass of each mission, and on the 21st of March the sensor was recording data across the coastline of the Nunivak island (see Figure 3-1). The Konganevik point located at 70° 5.12′ north latitude and 145° 9.9′ west longitude in the Camden Bay was used as a reference point for the imagery gathered on the 18th of March. This reference point is located at the end of the last pass of data gathered on this day, therefore, any error in the INS should be greatest at this point. This reference point revealed a discrepancy in the SAR's swath location of 3.5nm in longitude and 6.2nm in latitude which is less than half of the SSM/I footprint. The mean drift of the aircraft was computed as the total aircraft drift divided by the flight time to the reference point giving a mean drift for the 18th of March data of 0.93 knots, which is within the expected mean drift for the INS system used aboard the P-3 aircraft.

3.2 IMAGE DATA ANALYSIS

As mentioned previously, the SAR sea ice data collected on both the 18th and 19th of March 1988 during the Alaska survey is used to validate the multiyear ice concentration estimates generated from the SSM/I overflights, and the data gathered on the 21st of March is used to validate the total ice concentration estimates. The SAR ice concentration estimates are derived manually from a SAR photographic mosaic which was produced by optically processing the digital SAR data collected at C-band (5.30 GHz) VV-polarization. Figure 3-3 shows the photographic mosaic for the SAR data gathered on the 18th of March along

90-20542

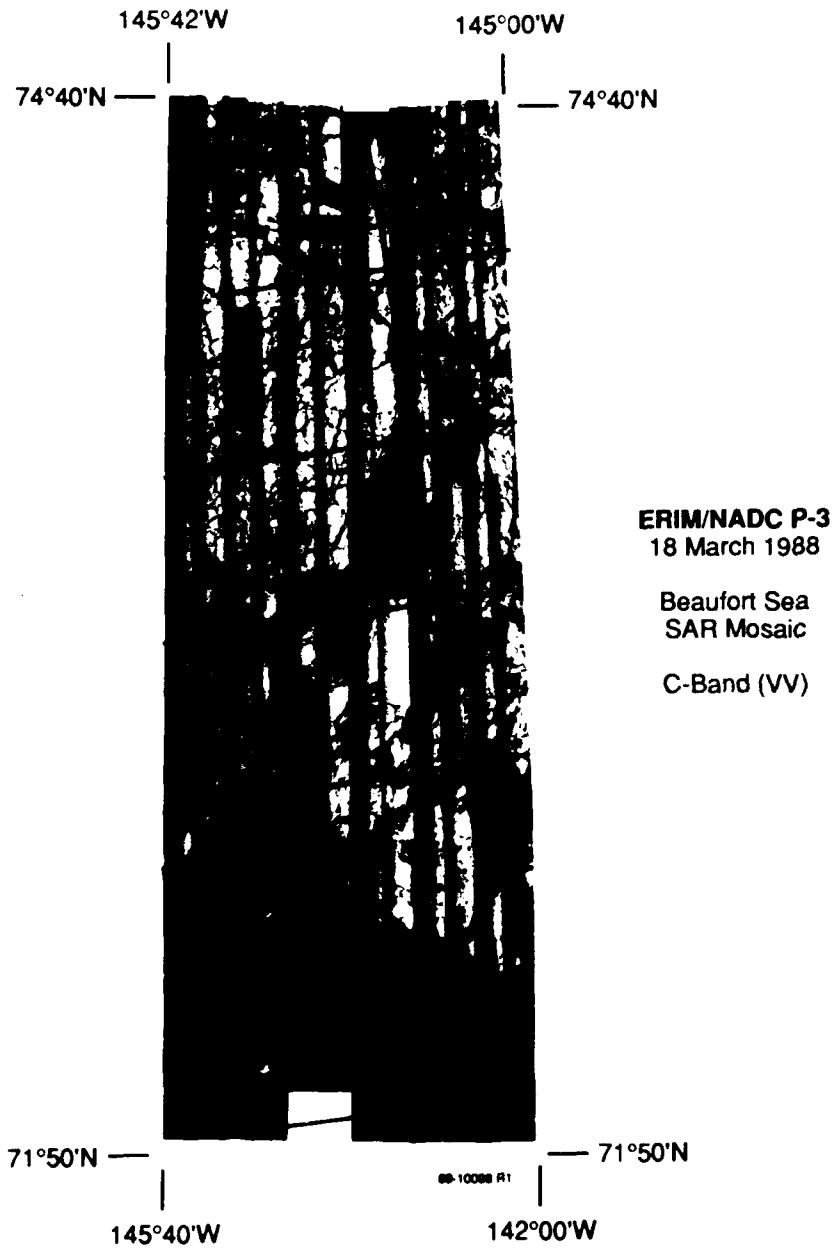

Figure 3-3. Photographic Mosaic of Digital SAR Data Collected in the Beaufort Sea on 18 March 1988. The Mosaic Shows the First-Year/Multiyear Ice Edge.

with boxes representing the SSM/I footprints (Figure 3-3 has been corrected for the location error described in section 3.1). Notice that this mosaic contains the first-year/multiyear ice edge which covers a wide range of multiyear sea ice concentrations. This allows us to analyze the SSM/I produced ice concentration estimates at the lower extreme values (i.e., no multiyear sea ice) as well as the high. Figure 3-4 illustrates the corrected SAR mosaic for the 19th of March data, again with the SSM/I footprints. This mosaic shows both first-year and multiyear sea ice located higher into the multiyear ice pack than the mosaic in Figure 3-3. Here, the mosaic contains a relatively uniform distribution of multiyear ice concentrations. Figure 3-5 gives the corrected SAR mosaic for the 21st of March data located on the southern coast of Nunivak island which appears to cross the boundary between the first-year sea ice and open water. As previously mentioned, the SAR data collected on both the 18th and 19th of March is used in the multiyear sea ice concentration comparison and the SAR data collected on the 21st of March is used in the total ice concentration comparison.

Each of the SSM/I footprints shown in Figures 3-3, 3-4, and 3-5 represent a 50 kilometer area on the ground. The SSM/I ice concentration estimates for each of these 50 kilometer areas is generated by averaging sea ice concentration estimates from four of the 25 kilometer SSM/I resolution cells. The SAR ice concentration estimates are derived from averaging 400 manually interpreted concentration estimates each covering a 2.5 kilometer area on the ground. The SAR estimates are produced by dividing each of the 50 kilometer SSM/I pixels into a 20 X 20 grid. Each of the 2.5 kilometer areas within this grid are then analyzed to determine the percentage of the desired sea ice concentration type (i.e., first-year ice, multiyear ice, and open water). The sea ice concentrations from all of the 2.5 kilometer areas within a given SSM/I box are then averaged to produce a single estimate which can be compared directly to the SSM/I ice concentration estimate. When the SSM/I pixels

90-20543

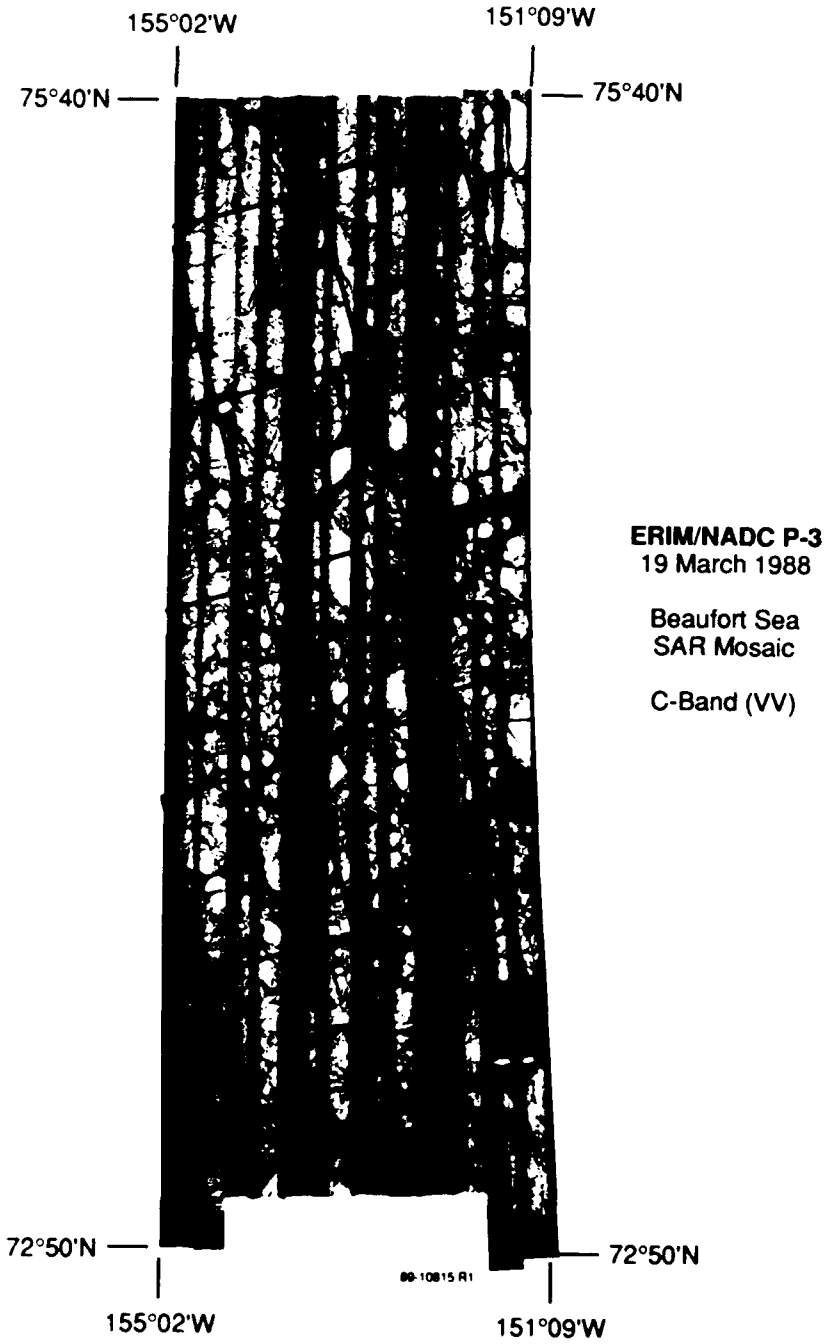

Figure 3-4. Photographic Mosaic of Digitial SAR Data Collected in the Beaufort Sea on 19 March 1988. The Mosaic Shows an Area of Both First-Year and Multiyear Sea Ice Located in the Multiyear Ice Pack.

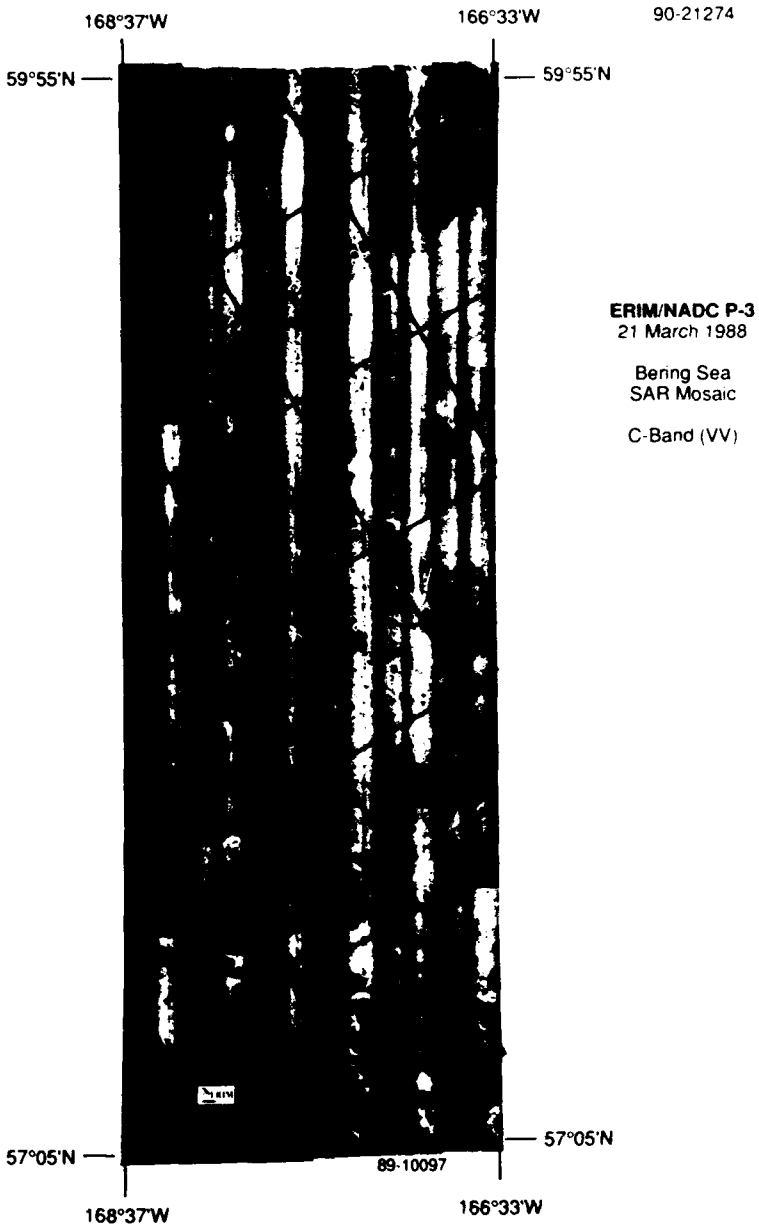

Figure 3-5. Photographic Mosaic of Digital SAR Data Collected in the Bering Sea on 21 March 1988. The Mosaic Shows the First-Year/Open Water Boundary

cross the SAR mosaic boundary (i.e., areas 3 & 4 of Figure 3-3, areas 3, 4, & 9 of Figure 3-4, and areas 1, 5, 8, 9, & 13 of Figure 3-5) the SAR ice concentration estimates reflect the average of only the 2.5 kilometer areas within the SAR mosaic boundary. Hence, the sea ice concentration estimates of these areas represent only the SSM/I pixel area with coincident SAR coverage. These estimates can be compared to the SSM/I estimates only after making the assumption that the partial areas outside the SAR mosaic boundary have ice concentration estimates consistent with the area within the SAR mosaic boundary.

The manually interpreted SAR ice concentration estimates produced for each of the 2.5 kilometer grid areas are averages of four separate manual interpretations by four different individuals and are rounded to the nearest 5 percent. Averaging the 2.5 kilometer areas should reduce the variance in the error associated with the manual interpretation. For this reason, the manually interpreted SAR ice concentration estimates are believed to be accurate to within plus or minus 5 percent. To check the validity of this error measure a digital concentration analysis was performed producing results which were well within the plus or minus 5 percent error previously stated. A discussion presenting the digital analysis algorithm along with the results of the digital analysis is given in section 4.1 of this report.

The SSM/I sea ice concentration algorithm used by the NASA/Goddard Space Flight Center is a multichannel algorithm which utilizes both the polarization and spectral gradient radiance ratios as independent parameters. This algorithm was developed by the NASA Team for the Nimbus project in the early 1970's. It was chosen to be the primary SSM/I ice concentration algorithm in 1985 by the NASA Sea Ice Algorithm Working Group (NSAWG) [10]. The NASA Team algorithm uses microwave polarization ratios (P_R) at a frequency of 19 GHz and a spectral gradient ratio (G_R) which utilizes the vertically polarized 19 and 37 GHz radiances to calculate the total (C_T), first-year (C_F), and multiyear (C_M) sea ice

concentrations. The polarization and spectral gradient ratios are defined as

$$P_R = \frac{TB_{V19} - TB_{H19}}{TB_{V19} + TB_{H19}} \tag{3-1}$$

$$G_R = \frac{TB_{V37} - TB_{V19}}{TB_{V37} + TB_{V19}} \tag{3-2}$$

where TB_V and TB_H are the vertical and horizontal brightness temperatures for the 19 and 37 GHz frequencies. The first-year, multiyear, and total sea ice concentrations can then be computed as

$$C_F = \frac{F_0 + F_1P_R + F_2G_R + F_3P_RG_R}{D_0 + D_1P_R + D_2G_R + D_3P_RG_R} \tag{3-3}$$

$$C_M = \frac{M_0 + M_1P_R + M_2G_R + M_3P_RG_R}{D_0 + D_1P_R + D_2G_R + D_3P_RG_R} \tag{3-4}$$

$$C_T = C_F + C_M \tag{3-5}$$

respectively, where F_i, M_i, and D_i (for i=0,1,2,3) are constants determined by the algorithm tie-point brightness temperatures. The tie-points used to generate the SSM/I sea ice concentration estimates are referred to as the "global" tie-points which are listed in Table 3-3. These tie-points are call the "global" tie-points because they are designed for mapping global ice concentrations. Table 3-3 actually contains two sets of tie-points, one for the northern hemisphere and one for the southern hemisphere. The reason for two sets of tie-points is due to the fact that sea ice signature variability can be considerable over different regions and for different seasons.

Table 3-3.
Global Tie-Points for the NASA SSM/I Sea Ice Algorithm

Freq & Pol (GHz)	Ocean	First-Year Ice	Multiyear Ice
Arctic			
19 H	97.7	236.0	203.9
19 V	175.3	254.0	223.2
37 V	199.6	250.0	186.3
Antarctic			
19 H	97.7	241.7	203.9
19 V	175.3	251.2	223.2
37 V	199.6	248.3	186.3

3.3 RESULTS OF COMPARISON

Table 3-4 shows the multiyear sea ice concentration estimates from the SAR and SSM/I data collected on both the 18th and 19th of March 1988. These estimates correspond to the ten coincident areas depicted on each of the mosaics shown in Figures 3-3 and 3-4. Notice that the ice concentration estimates generated for the 19th of March data are within 15% while much larger errors exist for the 18th of March data. Possible causes for these large ice concentration differences will be discussed in section 3.4. As mentioned previously, the SAR multiyear ice concentration estimates shown are averages of four separate manual interpretations by four different individuals and are believed to be accurate to within plus or minus 5 percent. Table 3-4 also contains the percent of SAR coverage for each of the ten coincident areas along with the difference in ice concentration estimates between the two sensors. This difference is computed as the SSM/I estimates minus the SAR estimate. The data in Table 3-4 shows that the difference in multiyear ice concentration is positive for every coincident area. Also, notice that the magnitude between the errors for both the 18th of March (where the imagery crosses the first-year/multiyear ice edge) and the 19th of March (where the imagery represents an area higher into the multiyear ice pack) is different, being much larger for the 18th of March data. The SAR ice concentration estimates are plotted against the SSM/I estimates for the 18th and 19th of March data in Figures 3-6, and 3-7 respectively. A linear regression was performed on the concentration estimates from both data sets giving the results illustrated in Table 3-5. The slopes of the linear regression are 0.69 and 0.79 with Y-intercepts of 33.16 and 18.27 for the concentration estimates from the 18th and 19th of March respectively. Since the correlation coefficient is relatively high (i.e., p=0.903) for the 18th of March comparison we must believe that the fitted line does represent the linear trend seen in the concentration estimates shown in Figure 3-6. This is unfortunate

Table 3-4.
SAR-SSM/I Multi-Year Ice Concentration Estimates Derived From
50 km Areas of Data Gathered During the March 1988 Alaska Survey

	March 18, 1988				March 19, 1988			
Area	% of SAR Coverage	SAR (%)	SSMI (%)	Dif (%)	% of SAR Coverage	SAR (%)	SSMI (%)	Dif (%)
1	100	0	37	37	100	58	64	6
2	100	6	41	35	100	55	62	7
3	80	27	57	30	80	57	58	1
4	100	6	28	22	82	52	66	14
5	100	48	50	2	100	52	55	3
6	100	48	66	18	100	49	57	8
7	100	40	62	22	100	57	68	11
8	100	56	78	22	100	72	74	2
9	100	47	69	22	91	56	60	4
10	66	55	74	19	100	64	73	9

ERIM

Multiyear Ice Concentration
18 March 1988

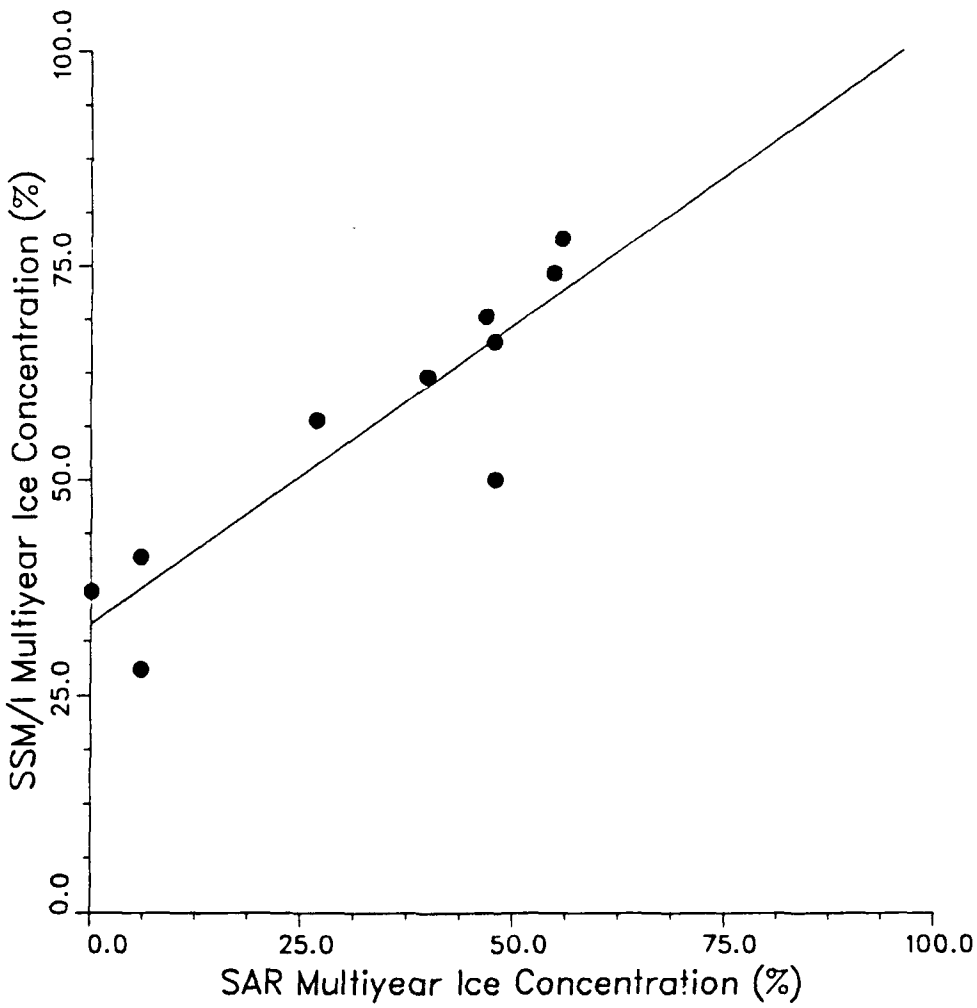

Figure 3-6. March 18, 1988 Multiyear Ice Concentration Estimates Plotted for Both the SAR and SSM/I Data Along With the Linear Trend.

Multiyear Ice Concentration
19 March 1988

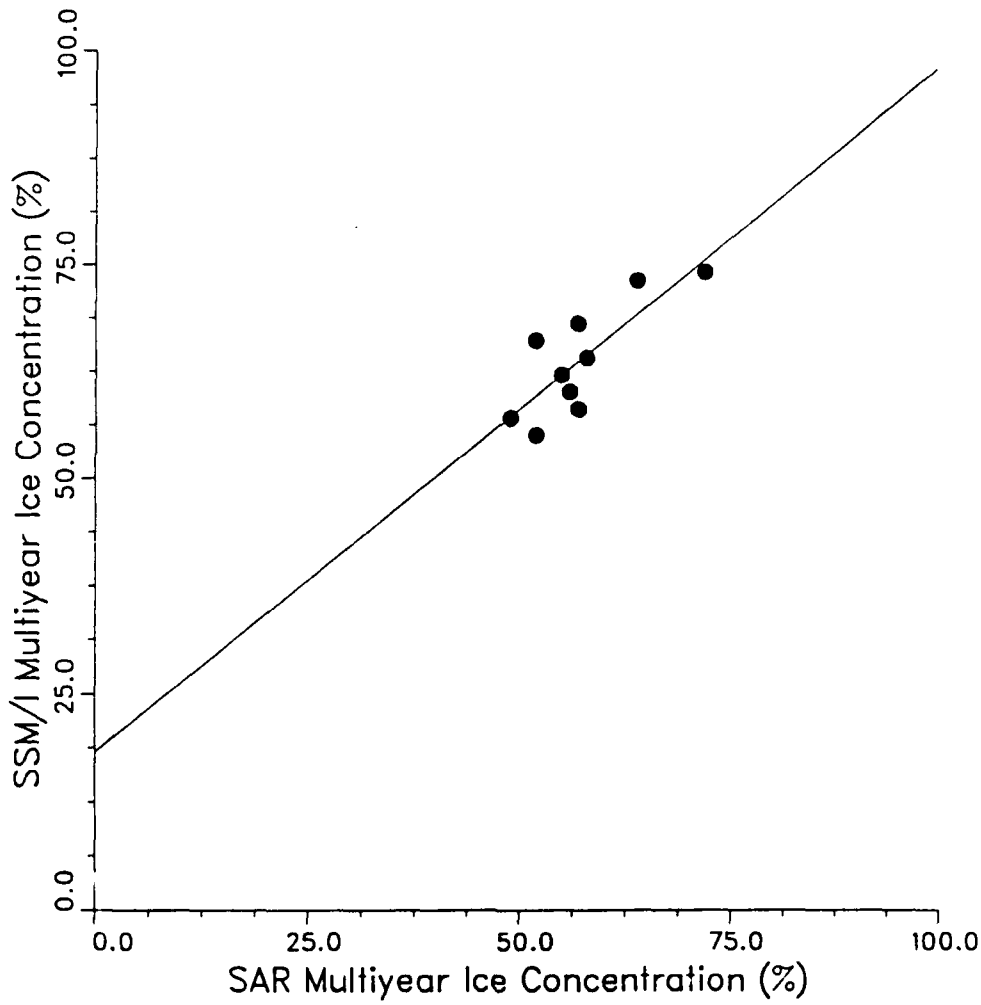

Figure 3-7. March 19, 1988 Multiyear Ice Concentration Estimates Plotted for Both the SAR and SSM/I Data Along With the Linear Trend.

Table 3-5.
Linear Regression Parameters for the Plots in Figures 3-6 and 3-7

Collection Data	Slope	Y-Intercept	Correlation Coefficient	MSE
18 March 1988	0.691	33.167	0.903	46.709
19 March 1988	0.794	18.271	0.802	13.783

because, if these concentration estimates were actually similar in value, they would be expected to propagate around a line with a slope of 1.0 and a Y-intercept of 0.0. It should be pointed out that the linear trend shown in Figure 3-7 representing the 19th of March comparison might not represent the actual trend in the data since the range of concentration estimates is relatively small. Therefore, the analysis of multiyear ice concentrations will focus on the results generated from the 18th of March data set. Figures 3-8, and 3-9 show the difference between the SSM/I and SAR multiyear ice concentration estimates (remember the difference is computed as the SSM/I estimates minus the SAR estimates) plotted against the SAR multiyear estimates for both the 18th and 19th of March data respectively. The results of the linear regression through these data points is given in Table 3-6. Again, since the concentration estimates computed from the 19th of March data are clustered around the 55 percent concentration mark with little variation, the linear regression might not represent the true trend in the data. However, the concentration estimates illustrated in Figure 3-8 do display a linear trend which is represented by the regression parameters given in Table 3-6.

The SAR imagery collected on the 21st of March is used to validate the SSM/I total ice concentration algorithm. Table 3-7 shows both the SAR and SSM/I total sea ice concentration estimates for the 21st of March data representing each of the thirteen coincident areas illustrated in Figure 3-5. As with the multiyear results given in Table 3-4, Table 3-7 contains the difference between both the SAR and SSM/I concentration estimates (computed as the SSM/I estimate minus the SAR estimate) along with the percent of SAR coverage for each of the SSM/I footprints. An interesting point to note from Table 3-7 is the fact that the SAR ice concentration estimates are larger than the SSM/I estimates for all except one of the coincident areas. Remember, the results of the multiyear concentration algorithm given in Table 3-4 showed the SSM/I concentration estimates larger than the SAR estimates for all of the

Multiyear Ice Concentration Error
18 March 1988

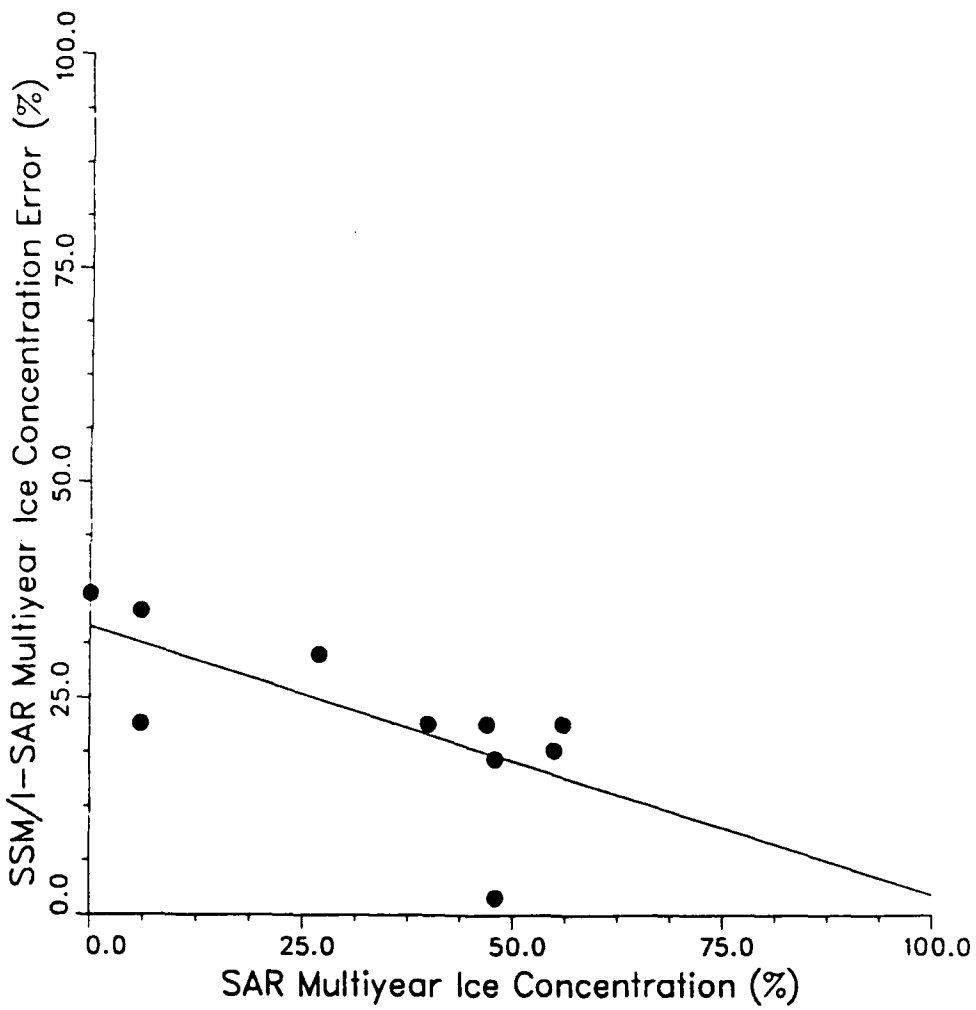

Figure 3-8. Multiyear Ice Concentration Error With Linear Trend Plotted for 18 March 1988 Alaska Data. The Error is Computed as the SSM/I Estimate Minus the SAR Estimate.

Multiyear Ice Concentration Error
19 March 1988

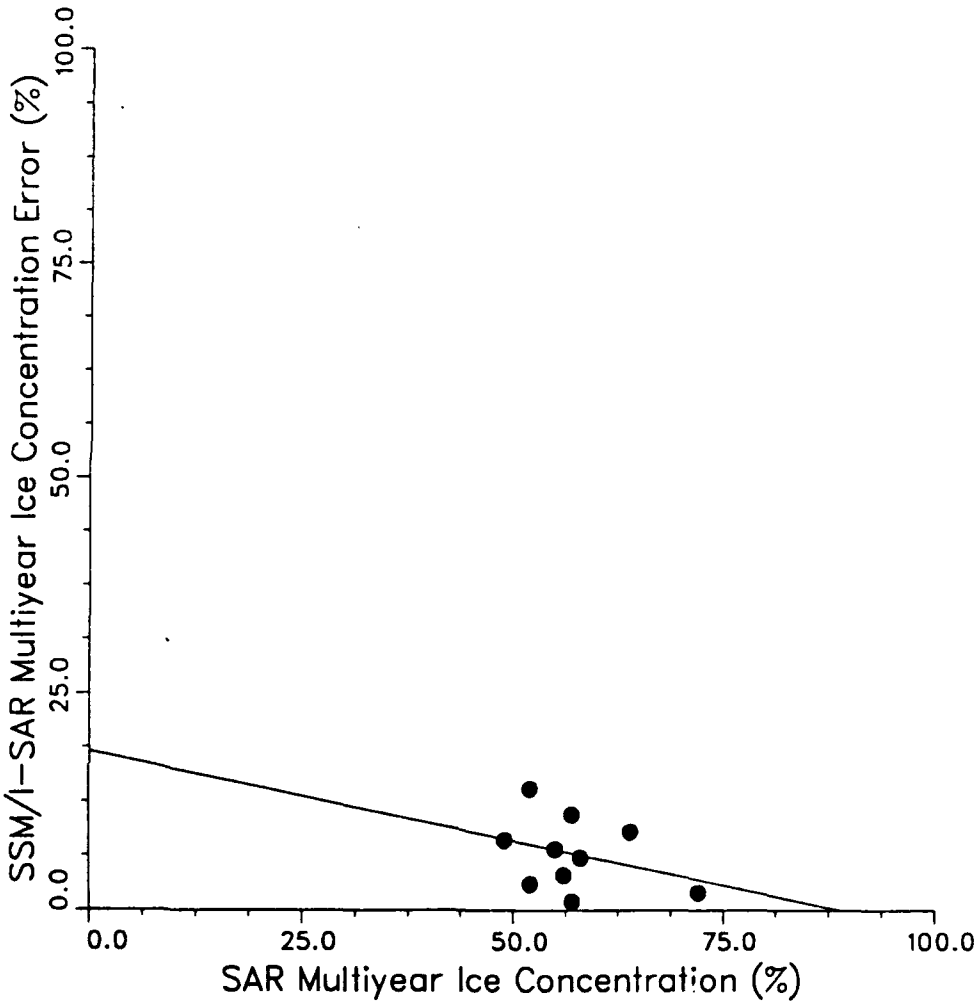

Figure 3-9. Multiyear Ice Concentration Error With Linear Trend Plotted for 19 March 1988 Alaska Data. The Error is Computed as the SSM/I Estimate Minus the SAR Estimate.

Table 3-6.
Linear Regression Parameters for the Plots in Figures 3-8 and 3-9.

Collection Data	Slope	Y-Intercept	Correlation Coefficient	MSE
18 March 1988	-0.308	33.167	-0.672	46.709
19 March 1988	-0.206	18.271	-0.328	13.783

Table 3-7.
March 21 1988
Lat. 57.10° - 59.90°
Long. 191.40° - 193.45°

Total Ice Concentration

Area	% Coverage of SAR	SAR	SSMI	Dif (SSMI-SAR)
1	65	59	38	-21
2	100	53	39	-14
3	100	53	57	4
4	100	86	72	-14
5	77	95	79	-16
6	100	99	86	-13
7	100	94	84	-10
8	84	97	86	-11
9	55	97	86	-11
10	100	97	84	-13
11	100	98	83	-15
12	92	80	61	-19
13	60	98	61	-37

RMS = 16.96

coincident areas on both the 18th and 19th of March data. A possible explanation for this switch will be addressed in section 3.4. Since the 21st of March mosaic contains the first-year/open water ice edge which excludes any multiyear sea ice, the total ice concentration estimates given in Table 3-7 actually represent the percentage of first-year ice in the imagery. Therefore, the total ice concentration algorithm Eq. [3-5] reduces to the first-year ice concentration algorithm given in Eq. [3-3] with the F_i's for i=0,1,2,3 being the tie-point brightness temperatures of first-year ice. The ice concentration estimates given in Table 3-7 are believed to be accurate to within plus or minus 5 percent for the same reasons as stated for the multiyear estimates. The SAR total/first-year ice concentration estimates are plotted against the SSM/I estimates in Figure 3-10. The results of the linear regression through these concentration estimates are illustrated in Table 3-8. Due to the relatively high correlation coefficient (p=0.87), one could argue that the line shown in Figure 3-10 really does represent the linear trend in the data. Table 3-7 shows that the linear trend in the data has a slope of 0.85 with a y-intercept of -2.25. The slope and intercept is quite close to that which would be expected from identical concentration estimates. These results imply that the total ice concentration algorithm does produce relatively accurate estimates, at least under the circumstances surrounding this data set. This can also be seen in Figure 3-11 which illustrates the total ice concentration error plotted against the SAR concentration estimates for the 21st of March data. The regression parameters for these data are given in Table 3-8. Notice the small negative slope indicating a small difference between the SAR and SSM/I total ice concentration estimates.

3.4 DISCUSSION

The purpose of this analysis is to use the high-resolution SAR imagery to determine the accuracy of sea ice concentration estimates

Total Ice Concentration

21 March 1988

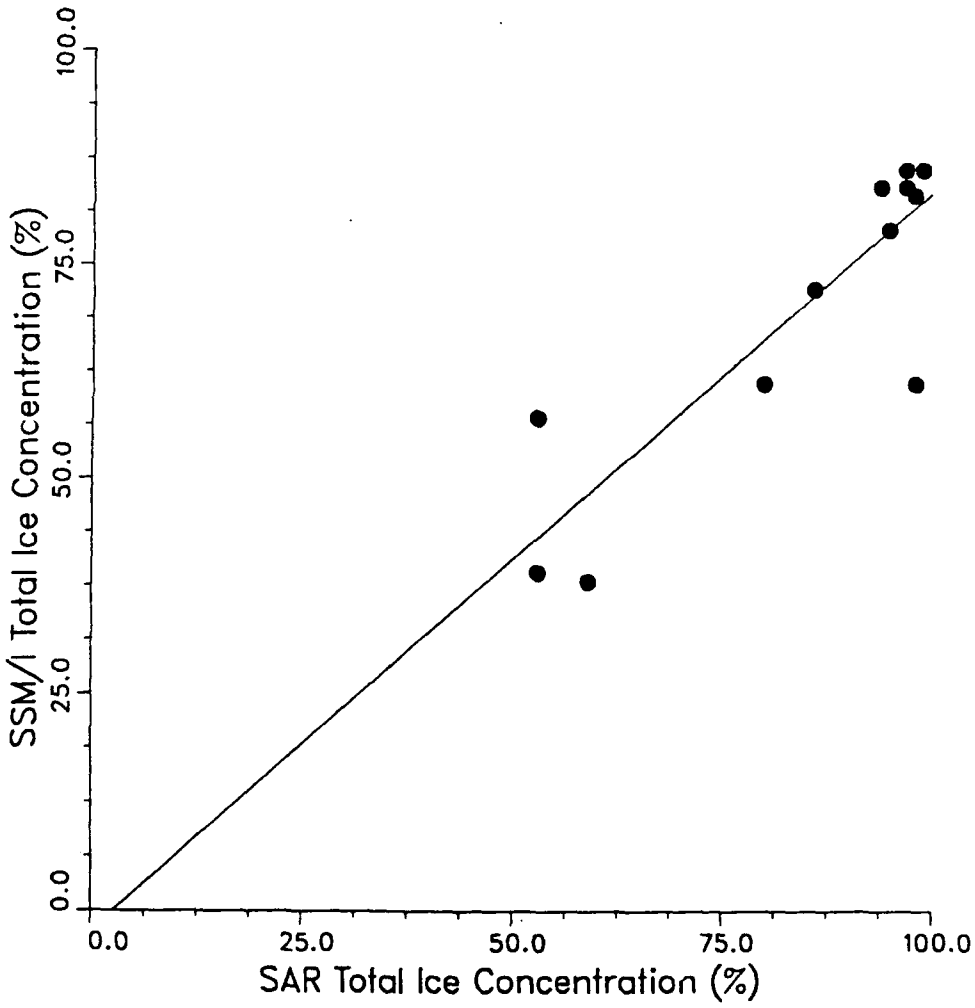

Figure 3-10. March 21, 1988 Total Ice Concentration Estimates Plotted for Both SAR and SSM/I Data Along With the Linear Trend.

Table 3-8.
Linear Regression Parameters for the Plots in Figures 3-10 and 3-11.

Figure	Collection Date	Slope	Y-Inter	ρ	MSE
3-10	21 March 1988	0.85	-2.25	0.87	67.75
3-11	21 March 1988	-0.15	-2.25	-0.29	67.75

Total Ice Concentration Error

21 March 1988

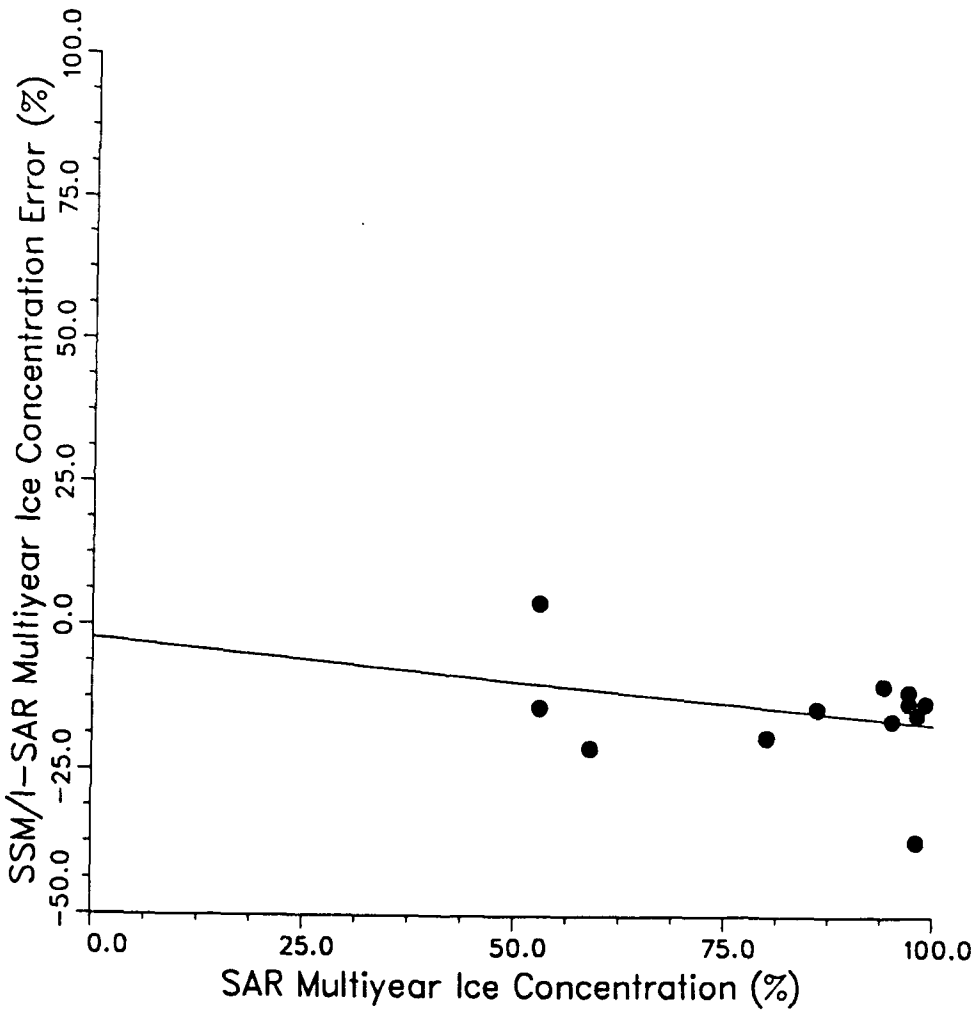

Figure 3-11. Total Ice Concentration Error With Linear Trend Plotted for 21 March 1988 Alaska Data. The Error is Computed as the SSM/I Estimate Minus the SAR Estimate.

produced from the NASA Team multichannel passive microwave ice concentration algorithm run on imagery generated from the SSM/I sensor. A previous comparison between the SAR and the ESMR imagery produced good results (rms errors within 14%) for estimates generated from a single-channel passive microwave ice concentration algorithm [2]. It is quite obvious from the results shown in section 3-3 that the SSM/I multiyear ice concentration estimates do not agree with the SAR estimates for the 18th and 19th of March Alaska data. However, the total ice concentration results for the 21st of March Alaska data do somewhat agree (rms error is 16.96%). A hypothesis for the differences seen between the SAR and SSM/I multiyear ice concentration estimates is that they are caused by an accumulation of three factors. These factors including: (1) an alignment error between coincident SAR and SSM/I pixel locations; (2) the fact that pressure ridges in the Beaufort Sea first-year ice might be misclassified as multiyear sea ice by the SSM/I concentration algorithm; and (3) the SSM/I sea ice concentration algorithm brightness temperature tie-points (the "global" northern hemisphere tie-points) are inaccurate for the region over which this comparison takes place.

As stated above, a possible explanation for the difference seen in the multiyear ice concentration estimates generated from the 18th of March data would be an accumulated error in the locations of both the SAR and SSM/I footprints. The concentration estimates generated from the 19th of March data do not show this large of an error (mean difference of 6.5 percent). However, this data is located higher into the multiyear ice pack where a relatively uniform distribution of both first-year and multiyear ice exist. Therefore, location errors would not have as severe an effect as in the area crossing the boundary separating first-year and multiyear sea ice. The mosaic representing the 18th of March data, illustrated in Figure 3-3, shows a monotonically increasing amount of multiyear sea ice with increasing latitude. This information was used to determine a possible shift in the SSM/I pixel locations which brought the mean difference between the multiyear concentration estimates down

to 9 percent from 23 percent. This shift corresponds to approximately 1 degree north in latitude and 1 degree east in longitude. Thus for location errors to be the cause of the multiyear ice concentration errors the location error would have to be on the order of 60 nautical miles which is rather unlikely.

Pressure ridges associated with the Beaufort Sea first-year ice are produced by the first-year ice expanding during the winter freeze. Since this first-year ice is wedged between the northern Alaska coastline and the multiyear ice pack, there is little room for it to expand. This causes the first-year ice to buckle producing ridges which are again frozen solid. These pressure ridges protrude above the first-year ice and are much rougher than the surface of the first-year ice. As the wind blows across the ice pack relatively large snow drifts build up around these pressure ridges. The snow covered pressure ridges then appear as volume scatterers altering the brightness temperatures measured by the SSM/I sensor (see Appendix A for more information on the effects of pressure ridges on the SSM/I microwave radiances). Our hypothesis is that pressure ridges in the first-year ice is being misclassified as multiyear ice by the NASA Team algorithm (due to the change in brightness temperatures measured by the SSM/I sensor). Since the ground area being imaged on both the 18th and 19th of March contains only first-ye and multiyear sea ice, Figure 3-8 and the corresponding regression parameters in Table 3-6 imply that 30 percent of the SSM/I multiyear concentration estimate is caused by the first-year ice in the image. Hence, 30 percent of the SSM/I multiyear concentration estimate is caused by the brightness temperatures produced from the pressure ridges contained within the first-year ice. A simple test was performed on the digital SAR data to determine if these pressure ridge lines could in fact constitute 30 percent of the energy within a given area of first-year ice. This test is based on the fact that the total energy received by the SSM/I sensor is the sum of the energy returned from both

the multiyear and first-year ice in the scene and can be modeled as follows:

$$E_t = pE_{my} + (1 - p)E_{fy} \tag{3-6}$$

where E_t represents the total energy received by the SSM/I sensor, E_{my} is the received energy caused by the multiyear sea ice in the scene, E_{fy} is the received energy caused by the first-year sea ice in the scene, and p is the percentage of the received energy classified as multiyear ice by the SSM/I sensor. The energy received by and area of first-year ice including pressure ridges is accounted for as

$$E_{fy} = E_{rl} + E_{fnr} \tag{3-7}$$

where E_{rl} is the received energy caused by the pressure ridge lines, and E_{fnr} is the received energy caused by the first-year ice without pressure ridges. When the SSM/I sensor is viewing an area containing only first-year sea ice (i.e., Area 1 on the 18th of March mosaic where the SAR multiyear estimate is 0 percent and the SSM/I estimate is 37 percent), equations 3-6 and 3-7 will be equal giving

$$E_t = E_{fy} \implies pE_{my} + (1 - p)E_{fy} = E_{rl} + E_{fnr}. \tag{3-8}$$

Therefore, the percent of received energy (caused by the pressure ridges in the first-year sea ice) being misclassified as multiyear ice by the SSM/I sensor is given as

$$p = \frac{E_{rl}}{E_{my} - E_{fnr}} = \frac{E_{fwr} - E_{fnr}}{E_{my} - E_{fnr}} \tag{3-9}$$

where E_{fwr} is the energy received from an area of first-year sea ice with pressure ridges. Assuming that the change in the SSM/I measured

brightness temperatures is proportional to the scattering effect measured by the SAR sensor, the digital SAR data can be used to compute an estimate of this effect. The displacement of these pressure ridges throughout the first-year ice made finding an adequate area of first-year ice without pressure ridges difficult. Therefore, the energy (measured as the SAR intensity return) associated with an area of first-year ice without pressure ridges was determined by thresholding an area of first-year ice to remove the pressure ridges. A visual inspection of the digital SAR image was used to determine the appropriate threshold location which would separate the pressure ridges from the first-year sea ice. Substituting the calculated values for E_{fwr}, E_{fnr}, and E_{my} into Eq. [3-9] for three separate areas generated the results shown in Table 3-9. Table 3-9 indicates that approximately 30 percent of the SAR energy received over three different areas of first-year ice in the Beaufort Sea is produced from the pressure ridge lines. Also, notice that the spatial extent of the pressure ridges over these three areas is slightly less than half of the energy contribution. This implies that a small amount of pressure ridge lines in an area of first-year sea ice produces a relatively large increase in received energy by the SAR sensor (and possibly the SSM/I sensor).

Another possible source of error could be due to selecting the "global" brightness temperature tie-points for the northern hemisphere as opposed to computing "local" tie-points for the ice concentration algorithm. By using the "globally" chosen tie-points for the calculation of ice concentration, the variation of open water, first-year ice, and multiyear ice brightness temperatures over both time and space are ignored. However, there are large variations in brightness temperatures caused by various effects including surface roughness (i.e., pressure ridges in Beaufort Sea first-year ice), foam and atmospheric water vapor content [5,6]. Since the accuracy of the NASA Team sea ice concentration algorithm is directly effected by the brightness temperature tie-points used [5,6], regionally computed tie-points might produce smaller errors

Table 3-9.

RESULTS OF PRESSURE RIDGE ANALYSIS

Area	Spatial Extent of Pressure Ridges	ρ
1	12.3 %	26.8 %
2	13.8 %	28.7 %
3	13.9 %	28.7 %

than those seen in section 3.3. This is especially true for the data sets used in this analysis since the first-year ice signatures are considerably different between the Beaufort Sea data which includes pressure ridges and the Bering Sea data which doesn't contain any pressure ridges. The lack of local tie-point data along with the absence of pressure ridges in the Bering Sea data could account for the shift in the ice concentration errors as mentioned in section 3.3 of this report (remember that the SSM/I estimates were larger than the SAR estimates for all of the coincident Beaufort Sea data and SAR estimates were larger than the SSM/I estimate for all but one area of the Bering Sea data).

4.0 SAR SEA ICE SEGMENTATION ALGORITHMS

Many different ice types exist within the polar region and the ability to distinguish between them is still an unsolved problem [11]. This is primarily due to the variation in surface scattering of similar ice types from one season to the next. Both first-year and multiyear ice types may appear identical during the summer months when the ice is melting, as opposed to the winter when subtle changes in different ice types are apparent [12]. Therefore, any automatic sea ice classification system will have to apply multiple algorithms compensating for the season in which the imagery is gathered. In addition to the season in which the imagery is gathered, the ice classification system will have to compensate for the presence of multiplicative noise (due to the coherent nature of the SAR sensor) that causes large overlaps between the returns from different sea ice types. However, this analysis will use SAR imagery gathered during winter conditions (March 1988 Alaska data) to verify both coarse and high-resolution sea ice classification algorithms. The coarse resolution algorithm uses SAR data which is highly multilooked to reduce the effects of the multiplicative noise inherent to all SAR imagery, while the high-resolution algorithm is designed to separate different sea ice types with the presence of speckle

This chapter is divided into two sections; 4.1 will present a description of the coarse resolution sea ice classification algorithm developed for separating multiple ice types, and section 4.2 will discuss a high-resolution segmentation algorithm which utilize both the tonal and textural information inherent to SAR imagery.

4.1 COARSE RESOLUTION SEA ICE CLASSIFICATION ALGORITHM

A complex SAR image contains both real and imaginary parts which can be considered to be normally distributed with zero mean and some

variance. The magnitude image produced from a complex image (i.e., the square root of the sum of the squares of both the real and imaginary parts) is by definition Rayleigh distributed. However, due to the presence of varying clutter fields in SAR imagery, the magnitude data is not a true Rayleigh distribution but is "Rayleigh like". This distribution is almost always unimodal for high-resolution SAR imagery even when the imagery contains different ice types. Therefore, a simple thresholding algorithm is not applicable to high-resolution SAR imagery since no simple method for directly determining threshold values is available. Typically, multiple iterations of some type of filtering operation needs to be applied to the imagery to reduce the multiplicative noise before any threshold values can be determined. A smoothing filter (i.e., averaging or median filter) has the effect of reducing the variance in the image while maintaining the mean. This reduction in image contrast (where contrast is defined as the image variance divided by the mean square) increases the separability between different ice types. As the number of smoothing filter iterations increase, the image variance will decrease giving the largest possible separation between different ice types as the number of iterations approaches infinity. The problem with this approach is finding a fixed number of iterations which will allow a segmentation algorithm to automatically determine threshold values that will adequately separate different ice types for images from varying geographical regions and collection geometries.

Figure 4-1 illustrates a coarse resolution digital SAR image gathered from the Beaufort Sea on the 18th of March 1988 during the Alaska collection. This image corresponds to the upper portion of area 8 with a small overlap into area 9 of the SSM/I footprints on the mosaic shown in Figure 3-3. The digital SAR image consists of three swaths of the P-3 SAR data covering approximately 30 kilometers in range (longitude) and 45 kilometers in azimuth (latitude). As mentioned in section 3.1, the P-3 SAR image resolution is approximately 3 meters in

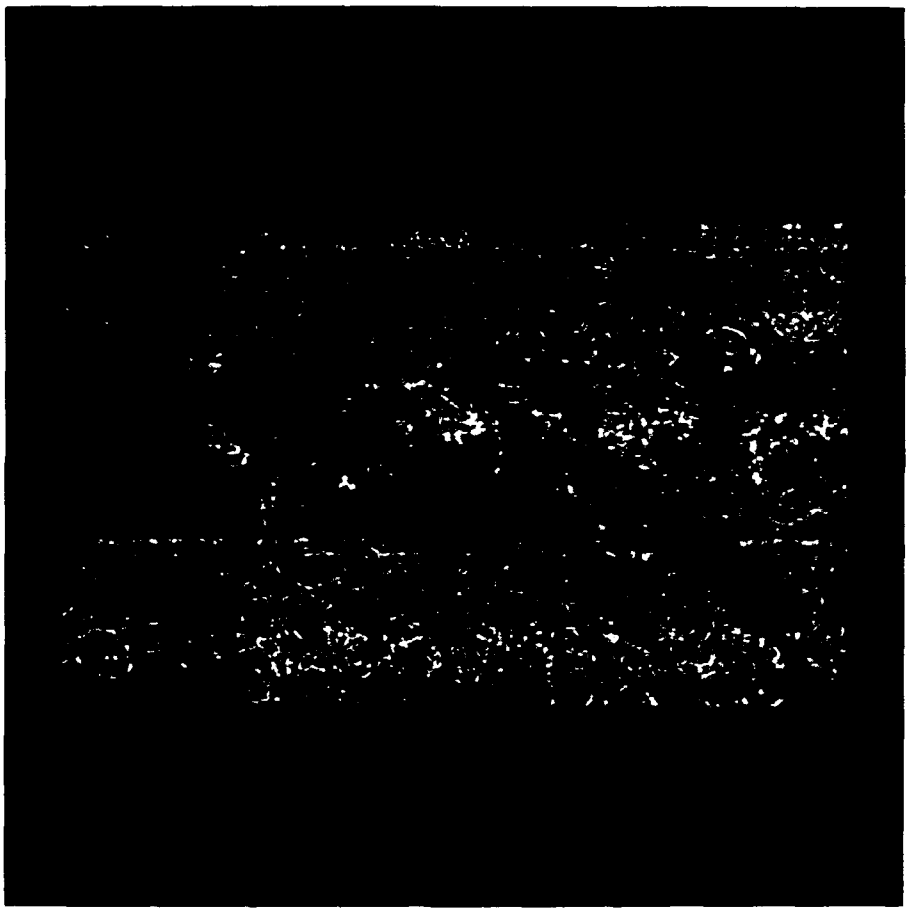

Figure 4-1. Coarse Resolution (Approx. 100 m Grid) SAR Image Corresponding to Area 8 of the March 18, 1988 Photographic Mosaic Shown in Figure 3-3. A Manual Interpretation of This Area Yielded 53% Multiyear Sea Ice.

both the range and azimuth directions. Therefore, the digital SAR image shown in Figure 4-1 represents approximately 150 million high-resolution SAR pixels which corresponds to about one half of a SSM/I footprint. However, the digital image shown in Figure 4-1 has been processed as real aperture radar data and averaged (multilooked) to a 100 meter grid. Also, notice that the image contains both first-year ice, including the pressure ridge lines, and multiyear sea ice. A manual interpretation (as discussed in section 3.2) was performed on this image which produced a multiyear sea ice concentration of 53% as illustrated in Figure 4-1.

As explained previously, averaging the high-resolution SAR pixels reduces the image contrast which improves the ability to separate the different ice types. A histogram of the coarse resolution digital SAR image shown in Figure 4-1 is given in Figure 4-2. Notice that this histogram is bimodal indicating a threshold value of 790 which will separate the SAR image into both first-year and multiyear sea ice. Figure 4-3 shows a binary segmentation map of the coarse resolution digital SAR image where the white and dark areas represent both multiyear and first-year sea ice respectively. Also, notice that the binary segmentation map yields a multiyear sea ice concentration contribution of 52.8% which is consistent with the 53% yield produced by the manual interpretation. Figure 4-4 illustrates another binary segmentation map of the digital SAR image after a nearest neighbor filtering operation was run on the binary map given in Figure 4-3. The nearest neighbor filter was run to remove isolated pixels, considered as noise spikes, to further improve the image segmentation process. Again, notice the multiyear sea ice concentration is 53.4% which is also consistent with the results of the manual interpretation.

4.2 HIGH-RESOLUTION SEA ICE CLASSIFICATION ALGORITHM

In the immediate future a number of SAR satellite sensors will be launched whose coverage will include the arctic regions. The massive

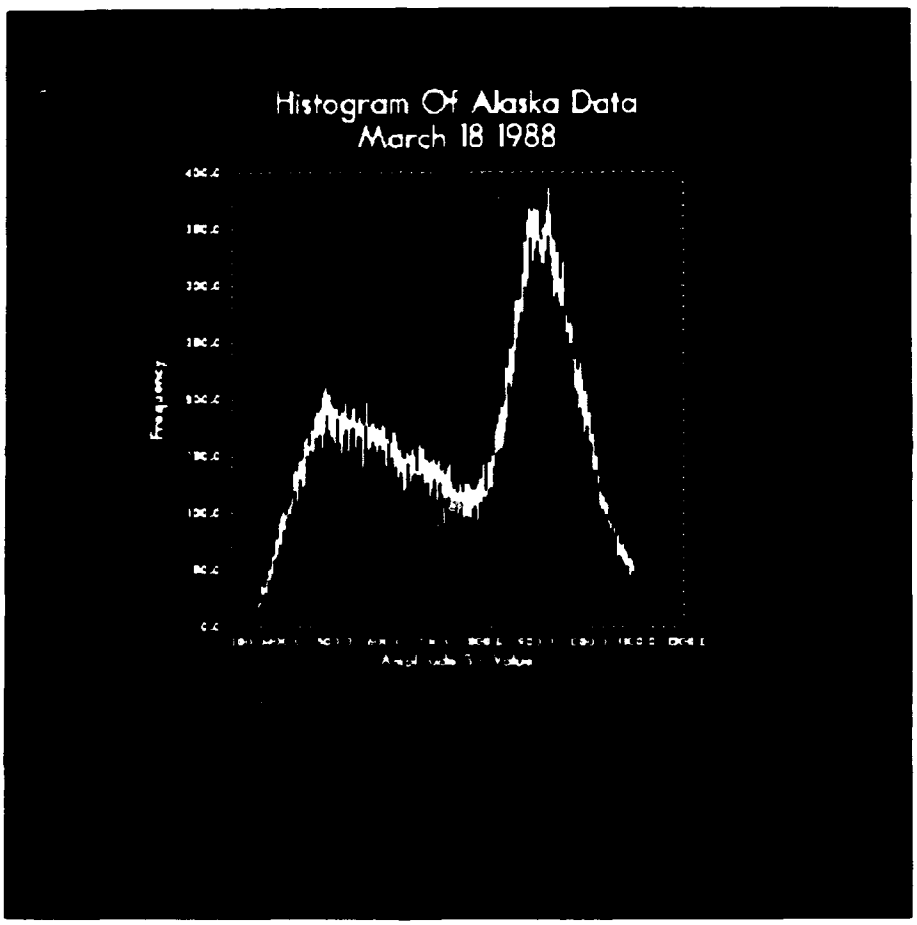

Figure 4-2. Histogram of the Coarse Resolution SAR Image Given in Figure 4-1. Bimodality of Histogram Suggests a Threshold Value Which will Seperate the Two Ice Types.

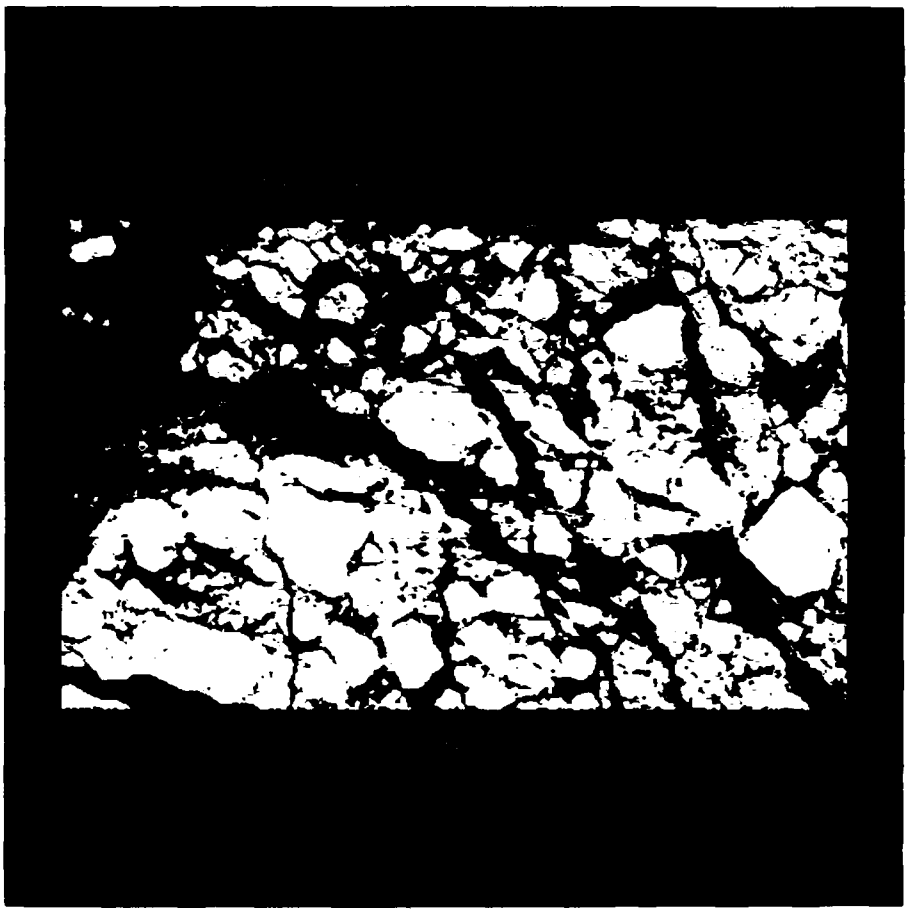

Figure 4-3. Binary Map of Coarse Resolution SAR Data Thresholded at 790. Multiyear Ice Concentration is 52.8%.

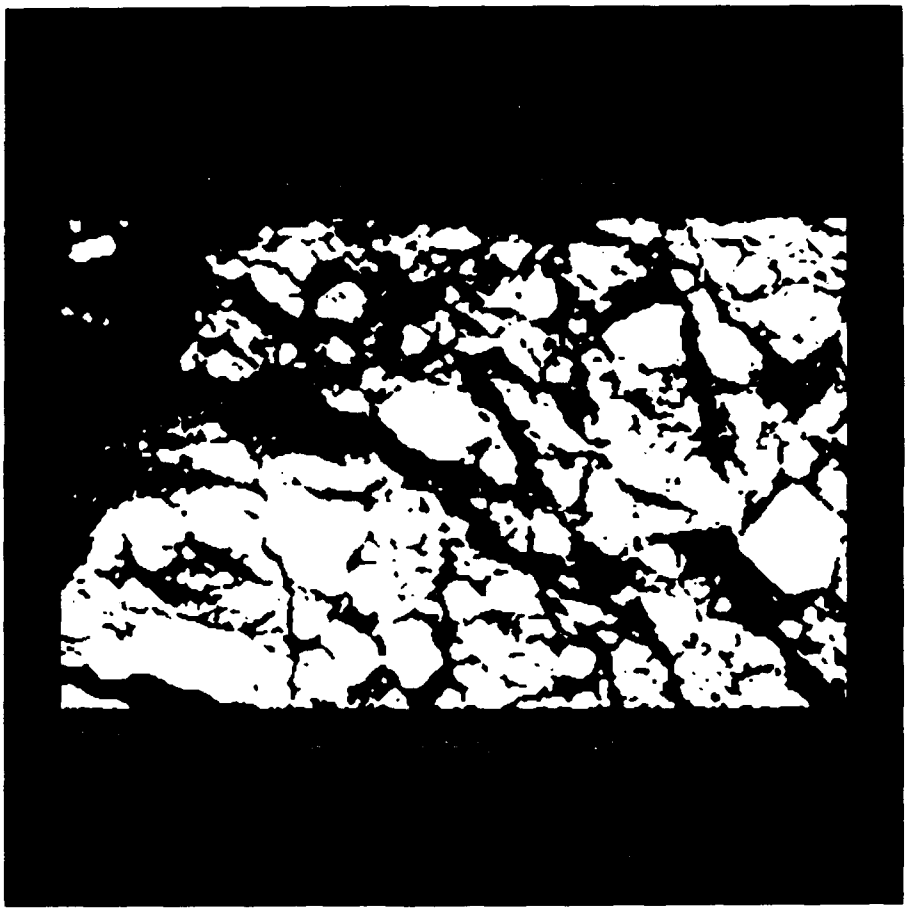

Figure 4-4. Binary Map of Coarse Resolution SAR Image After a Nearest Neighbor Operation was Performed to Remove Isolated Pixels. Multiyear Ice Concentration is 53.4%.

amounts of data that these sensors will generate make automatic algorithms for turning the SAR image data into ice information maps essential. Such algorithms almost always have as their first step the classification of ice types and then derive from these ice type maps the information that is desired: ice concentration, lead formation, ice motion, ice edge location, etc. The current classification algorithms generally calculate a feature from the SAR image data first, and then threshold the feature values to determine ice type; two of the most common image features being first order statistics and image texture derived from a general co-occurrency matrix. It is not known currently however how well the existing algorithms perform on an absolute scale, that is whether they generate optimum separation of the ice classes, or even which image feature is best for classification. One attempt to answer these questions would be to generate a procedure for estimating the optimal combination of a given set of image features to achieve maximal separation of the resulting classes. Although such a procedure would not in general provide an ice classification algorithm (the resulting combination of features may be different for each image), it would provide a benchmark for existing algorithms as well as a method of ranking different sets of feature vectors.

Such a goal is very noble, but very difficult, and thus, as a first step, we limited ourselves to only linear combinations of the image features. This limited problem has been solved before, and the solution will be described in Section 4.2.1. To increase the scope slightly, we will expand the image feature set by including ratios of the original measures or squares of the original measures. In Section 4.2.2 we will generate this benchmark for two types of image features: first order statistics up to the fourth power, and texture measures derived from the co-occurrency matrix. This will be done for two SAR image sets; one from the Greenland Sea which contains open water, first-year ice, Odden ice, and multiyear ice, and one from the Beaufort Sea

which contains first-year ice and multiyear ice only. Finally, Section 4.2.3 will present a summary and conclusions.

4.2.1 Optimal Algorithm

We will assume that we have extracted a series of subsets from SAR image data where some of the subsets are taken from a known ice type, some from another ice type, etc. For each subset we assume that we have generated a vector of measurements which we will denote by δ. We will thus have a set of vectors from each ice type. Given another vector, υ, we could form the dot product between υ and each of the measurement vectors to form a set of scalar values, p, for each ice type. We will define a clustering metric, c, for the values of p as

$$c = (\sigma^2 - \Sigma\sigma_i^2)/\Sigma\sigma_i^2 \tag{4-1}$$

where σ_i^2 is the variance of the scalar values p for the ith ice type, σ^2 is the variance of the scalar values p for the entire data set (i.e., over all of the ice types), and the summations are over the different ice types in the data set. If c is large, then for those p values the ice classes are well separated since the distance between classes (the numerator) is large compared to the size of each class (the denominator).

We can now state our goal precisely; given a set of measurement vectors, δ, find the vector υ such that the resulting clustering metric, c, defined by Eq. (4-1) is maximal. The vector υ will then represent the optimal combination of measurements to maximally separate the ice classes. We can generate an explicit expression for υ [14,15] by noting that $\sigma_i^2 = \upsilon^t C_i \upsilon$ and $\sigma^2 = \upsilon^t C \upsilon$ where C_i is the covariance matrix of the measurements from the ith ice class, C is the covariance matrix of the entire data set, and υ^t represents the transpose of υ. This allows us to re-write Eq. (4-1) as

$$c = (\upsilon^t B \upsilon)/(\upsilon^t W \upsilon) \tag{4-2}$$

where B is the so called between scatter matrix defined as $B = C - \Sigma C_i$ and W is the so called within scatter matrix defined as $W = \Sigma C_i$. From Eq. (4-2) it is simple algebra to generate

$$c\upsilon = W^{-1} B \upsilon \tag{4-3}$$

where W^{-1} indicates the inverse of W. It is clear from Eq. (4-3) that the vector which maximizes c is the eigenvector of the matrix $W^{-1}B$ with the maximal eigenvalue; since the eigenvalue will in fact be c.

One immediate problem apparent in Eq. (4-3) is that the inverse of W is needed. It is possible for W to be singular, and in fact in many cases we found that it was. What this implies is that the elements of the measurement vector are not independent; i.e., we have too many measurements. However, since all we are using Eq. (4-3) for is to generate a linear combination, we can first "whiten" W, then perform our analysis, then "unwhiten" the result. Specifically, this entails finding all of the eigenvectors of W and forming the dot product of each measurement vector with each eigenvector. This generates a new measurement vector for each subset for which the new W matrix will be diagonal (i.e., "whitened") and invertible by definition. After finding the optimal υ in this new domain, we can convert back to the original domain.

4.2.2 Data Results

We applied this procedure to two of the more common image features that are used to classify ice types; first order statistics and texture measures. For the first order statistics we used up to the fourth power, and normalized them in two different ways. The first set of measurements was: $E[x]$, $(E[x^2])^{1/2}$, $(E[x^3])^{1/3}$, $(E[x^4])^{1/4}$. This kept the measurements

within the same range, but was sensitive to scale factor changes between the images; i.e., the images had to be relatively calibrated with respect to each other. To remove this sensitivity we also examined a three element measurement vector which consisted of the last three elements of the above vector divided by E[x]. Unfortunately this vector never performed well, so we will not consider it further. For the texture measurements we used a co-occurrency matrix and derived from it six of the more common metrics: inertia, cluster shade, cluster prominence, local homogeneity, energy, and entropy [16]. We used a 20 X 20 co-occurrency matrix and derived all of the metrics from the bin numbers (i.e., 1 through 20) instead of the actual SAR image values. This made the resulting measurements insensitive to scale factors between the images. A co-occurrency matrix also requires a displacement vector and to determine this we generated the texture measures for a range of displacement vectors within a distance of 3 samples and picked the best. As can be seen below, we found no consistency in the optimal displacement vector.

We have examined two sets of SAR images to date. The first was from the MIZEX '87 collection and used the STAR 2 radar. The images were all X-VV and four ice classes were extracted: open water, first-year, multiyear, and Odden. The images were 7 looks and approximately 16 meter resolution. The second set was from the Alaska '88 collection and used the NADC/ERIM P-3 SAR. The images were all C-VV and only two classes were extracted: first-year and multiyear. The images were 4 looks and approximately 3 meter resolution. As mentioned in Section 1, in addition to the measurement vectors described above we also increased the vector length by adding either all possible ratios of the original measurements, or all possible multiplication of pairs of the original measurements. Obviously we could have continued to higher powers, but the computational cost became prohibitive. We found in all cases that the ratios performed the best of any of the measurement vectors, and so we will describe only those results.

Figure 4-5 shows a plot of the resulting p values for the optimal u using ratios of the first order statistics. The y-axis simply separates the p values for the four different ice types and the p values are plotted on the x-axis. Except for a single first-year value, Figure 4-5 shows a good separation of open water from all of the other classes, however not much separation is shown between the other classes. Figure 4-6 shows the same plot for the ratios of texture measures where the displacement vector was 3 X 3; note the much cleaner separation of open water. Figures 4-5 and 4-6 indicate that the difference between open water and the other classes may be masking the subtler differences between the other classes, so we discarded the open water data and re-analyzed the resulting three classes. Figures 4-7 and 4-8 show the statistics ratios and the texture ratios (this time for a displacement vector of 3 X 2), respectively, for the remaining three classes. The statistical measures indicate a fair amount of overlap between the classes, whereas the texture measures show a much cleaner separation although with slight overlap.

Figures 4-9 and 4-10 show the results for the Alaska data set. With only the two ice types, both measurements do a good job with the statistical measures being slightly better. The texture measures displacement vector here was 1 X 3.

Table 4-1 shows the clustering metric for all six of the measurement vectors analyzed and for each data set. Under the MIZEX data both the four class and three class analysis are shown. Table 4-1 indicates that the ratio of the original measurements always performed the best, and that the texture measures performed best for the MIZEX data while the statistics performed best for the Alaska data. However, the texture measures performed adequately for the Alaska data too, and thus seems the best choice among those tested.

Ratios of Statistic Measure

4 Classes

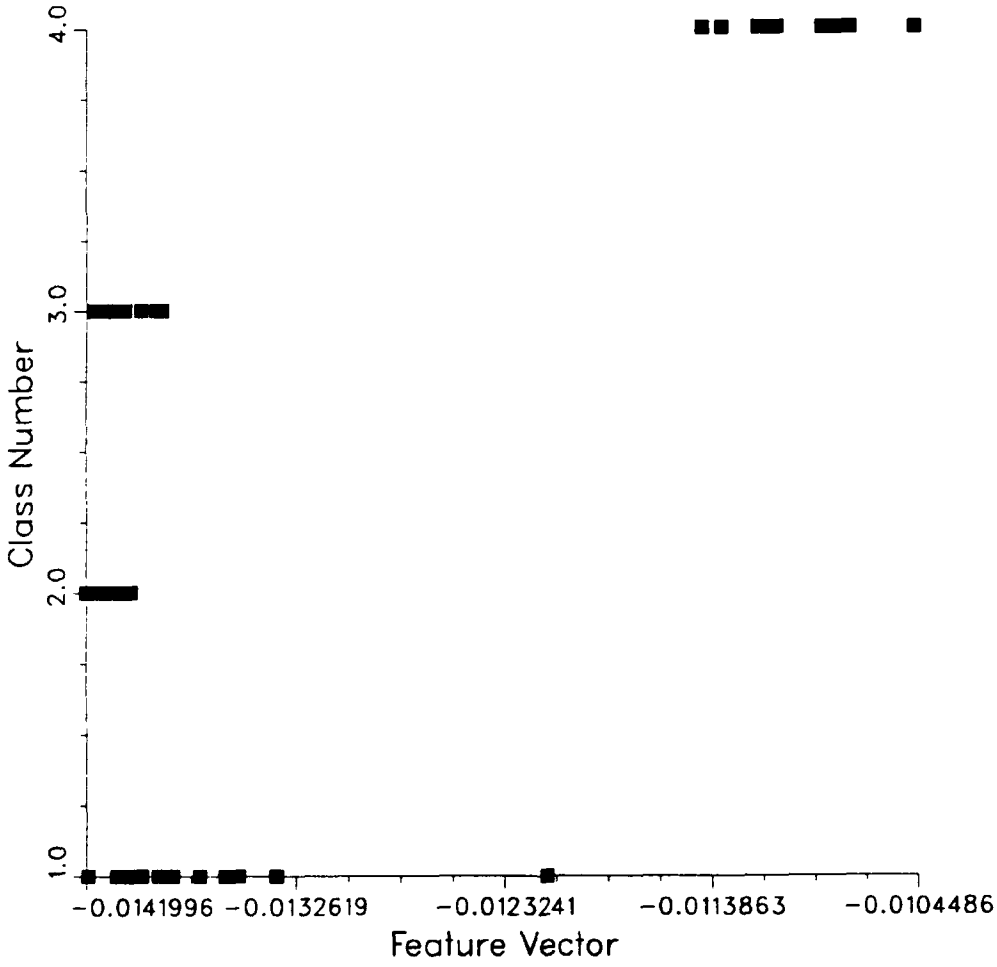

Figure 4-5. Optimal Combination of Ratios of Statistical Measures for MIZEX Data.

Ratios of Texture Measure

4 Classes Vector: X=3 Y=3

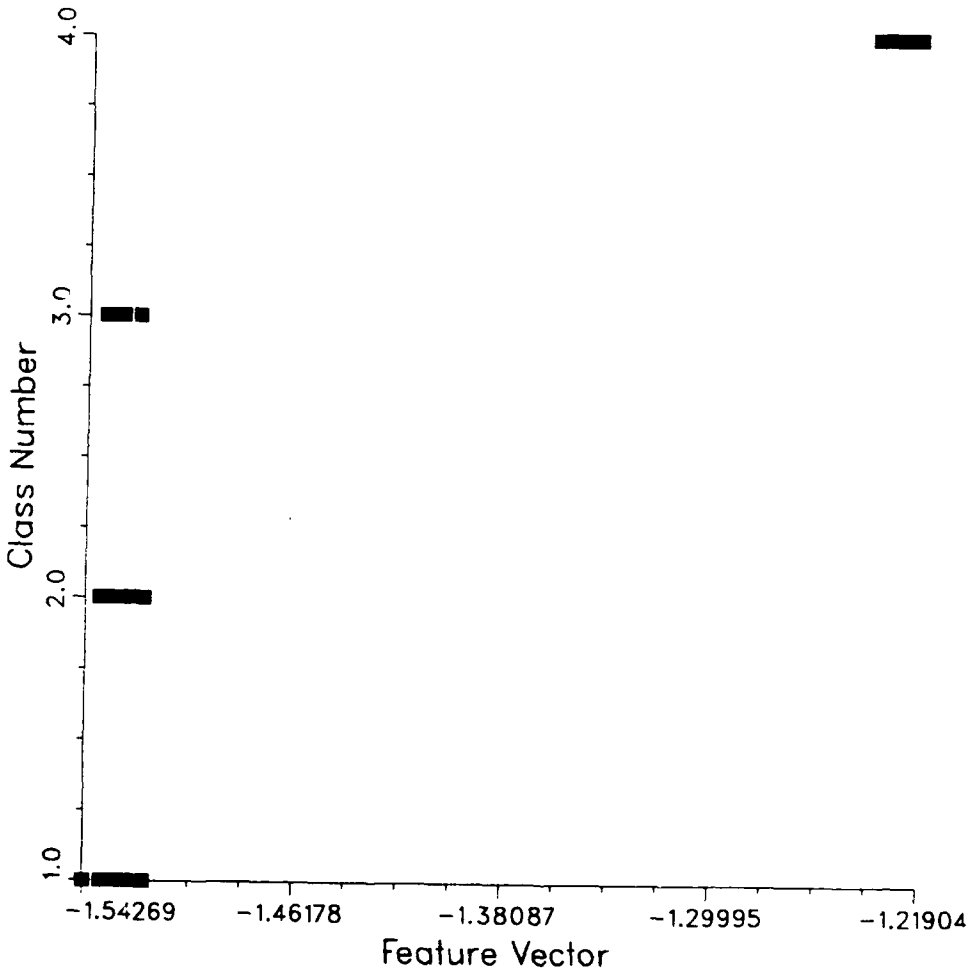

Figure 4-6. Optimal Combination of Ratios of Texture Measures for MIZEX Data.

Ratios of Statistic Measure

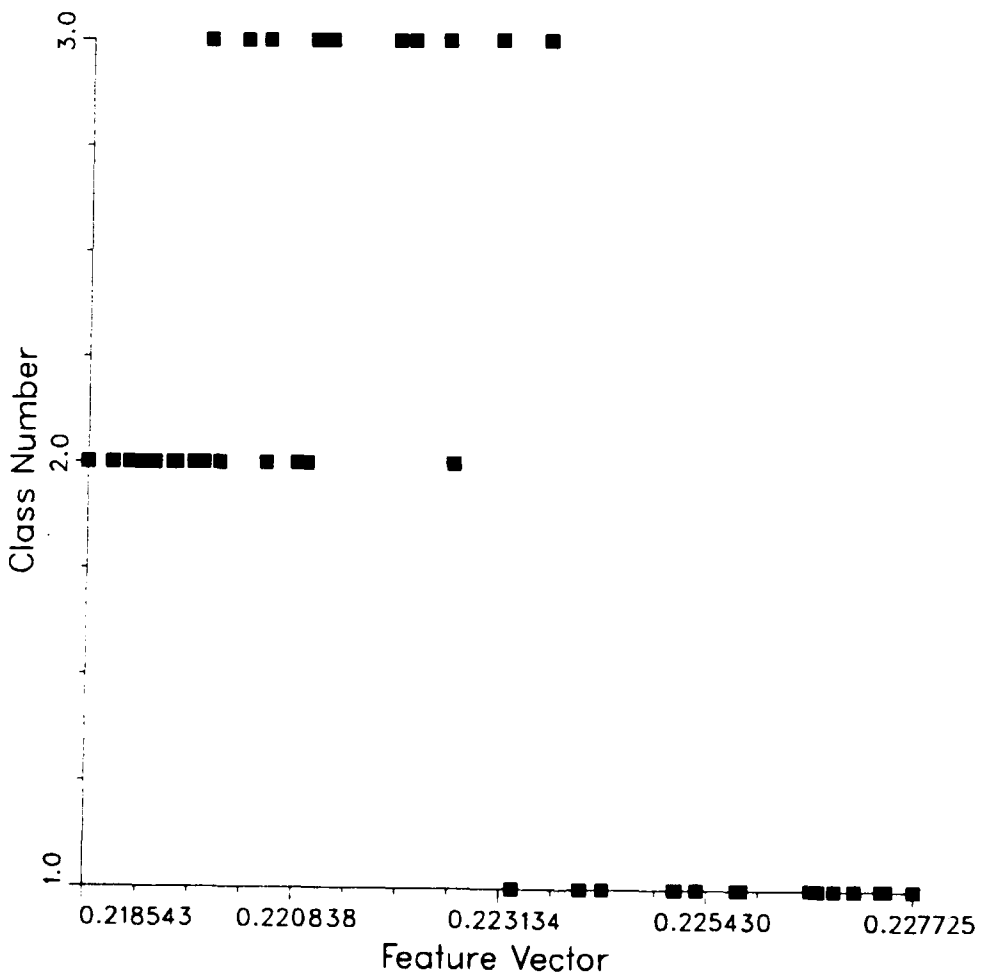

Figure 4-7. Optimal Combination of Ratios of Statistics Measures for Only Three Classes of MIZEX Data.

Ratios of Texture Measure

3 Classes Vector: X=3 Y=2

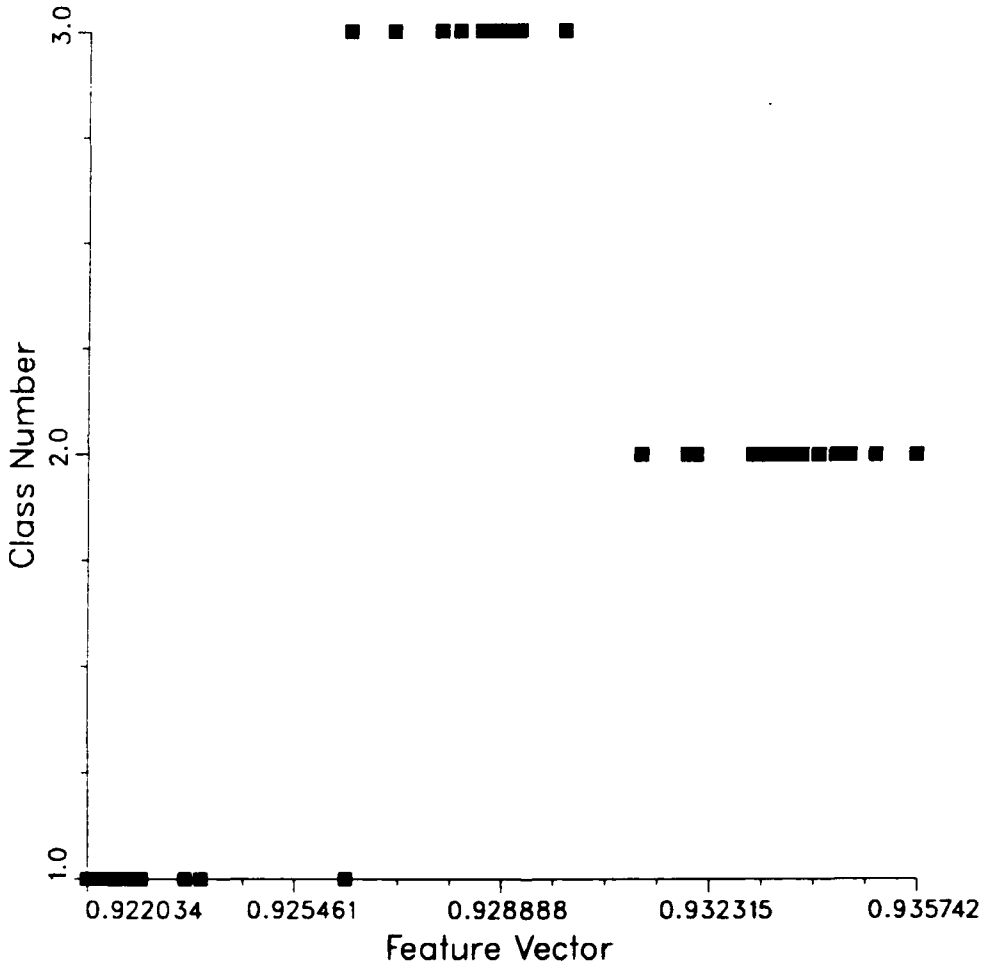

Figure 4-8. Optimal Combination of Ratios of Texture Measures for Only Three Classes of MIZEX Data.

Statistic Measure

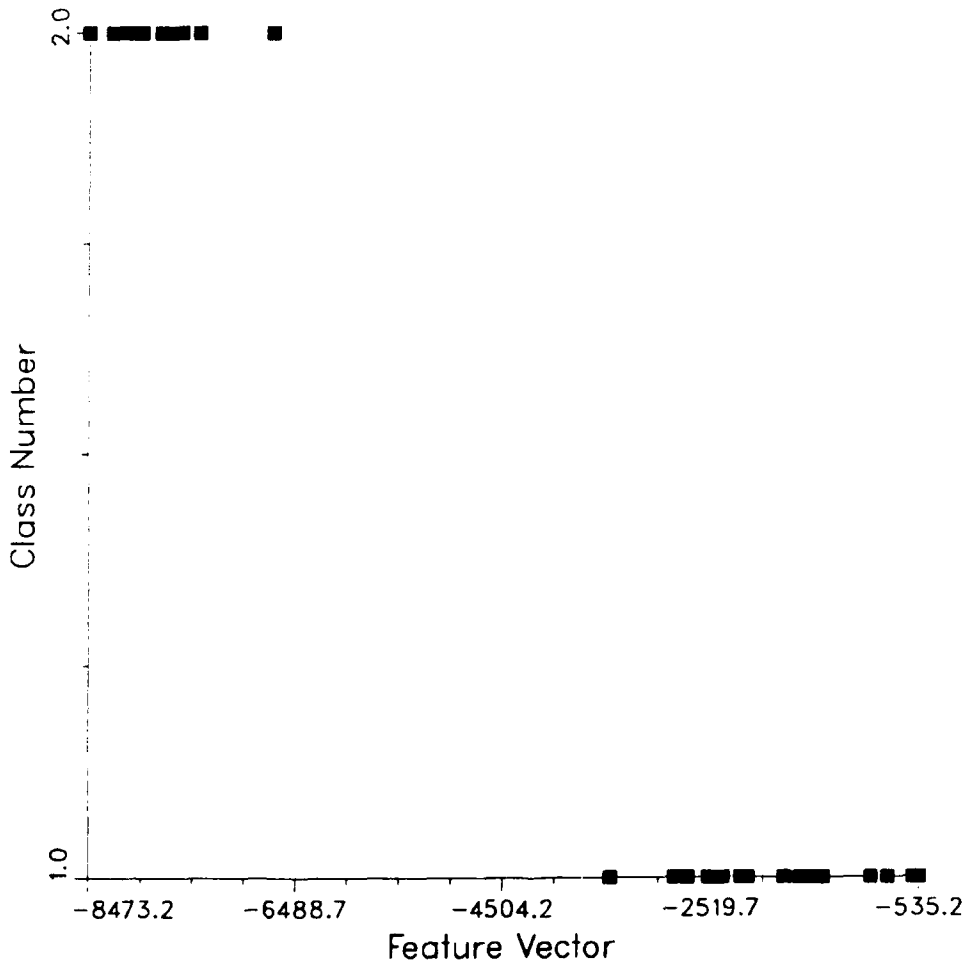

Figure 4-9. Optimal Combination of Ratios of Statistics Measures for Alaska Data.

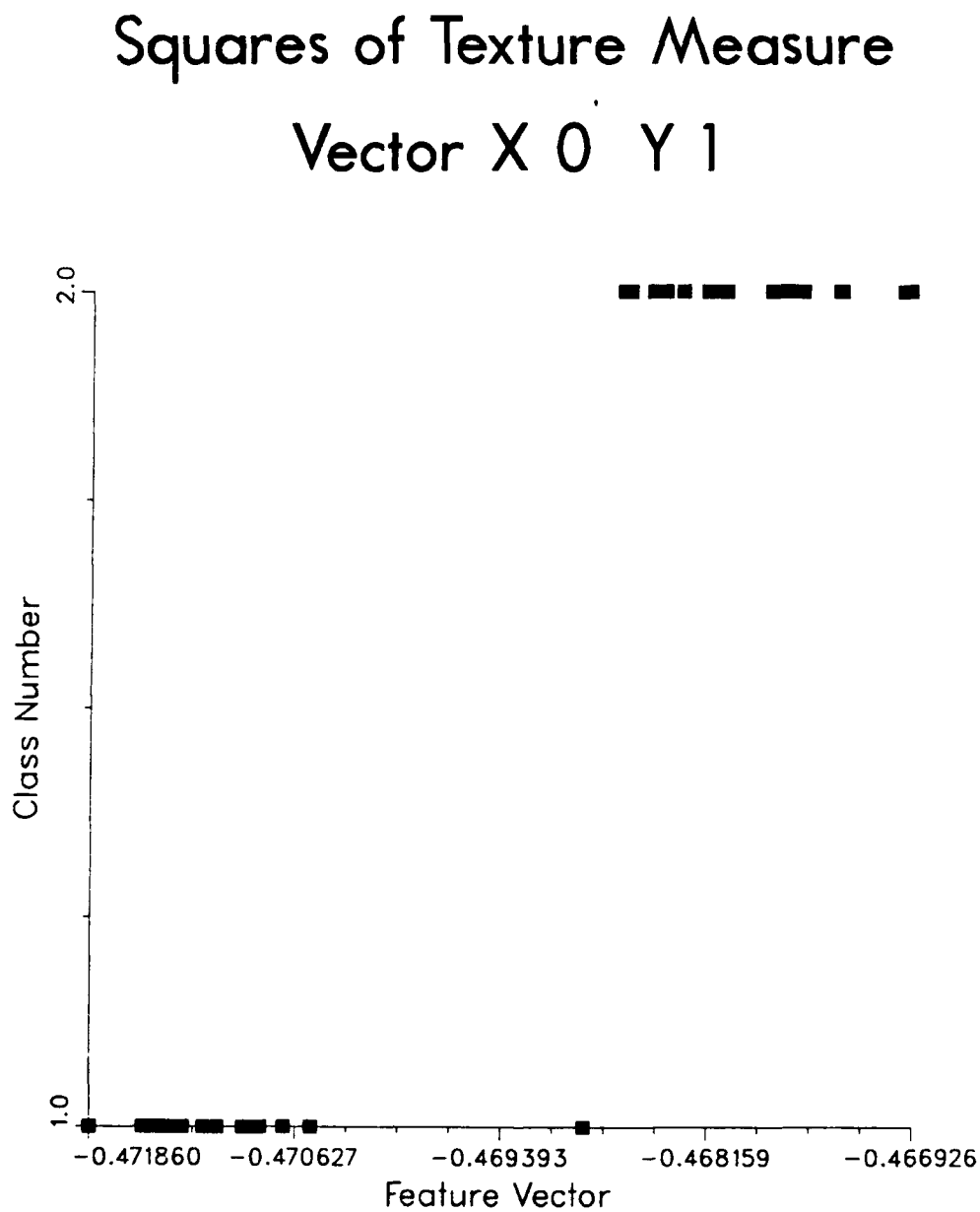

Figure 4-10. Optimal Combination of Ratios of Texture Measures for Alaska Data.

Table 4-1.
Optimal Clustering Metric for Each Measurement Vector and Data Set.

CLUSTERING METRIC

	MIZEX		ALASKA
	4 Classes	3 Classes	
Stats	.14	-.030	10
Stats-Ratio	4.5	1.1	21
Stats-Squared	.88	.35	20
Texture	4.3	.33	.33
Tex-Ratio	160	6.3	9.7
Tex-Squared	10	2.3	2.1

4.2.3 Summary and Conclusions

In order to derive both a benchmark for existing classification algorithms as well as a ranking of image features for their ability to classify, we have presented a procedure that generates the optimal linear combination of measurements to maximize the separation of the resulting classes. We have applied it to two of the more common features, first order statistics and texture measures, and found that the best separation came from ratios of the original measurements. We also found that the texture measures performed best overall for the two data sets we examined.

Before these conclusions can be made more forcefully however, we will need to perform more analysis on the same data to determine the robustness of the eigenvector results. In addition, we need to compare these results to some of the more common algorithms. Both of these analyses are currently being pursued.

5.0 CONCLUSIONS

The multiyear ice concentration estimates produced from the multi-channel NASA Team ice concentration algorithm do not agree with multiyear estimates generated by a manual interpretation of the SAR photographic mosaic data gathered during the March 1988 Alaska collection. The SSM/I multiyear estimates where higher than the SAR multiyear estimates for all twenty coincident Beaufort Sea areas containing a combination of both first-year and multiyear sea ice. However, the total ice concentration results derived from the March 21st data do somewhat agree (rms error is 16.96%). The SAR total ice concentration estimates were higher than the SSM/I total ice estimates for all but one area in the Bering Strait. Assuming the SAR estimates are correct, a possible explanation for this difference include: (1) an alignment error in the footprint locations between the SAR and SSM/I data; (2) the fact that pressure ridges associated with first-year sea ice might be misclassified as multiyear sea ice by the NASA Team ice concentration algorithm; and (3) the NASA Team ice algorithm brightness temperature tie-points are not adequate for the arctic region covered in this experiment. The backscatter energy produced by the pressure ridges in the digital SAR data closely correspond to the 30 percent difference seen in the March 18th ice concentration results. Also, a 1 degree error in the SSM/I pixel locations seem to account for the discrepancy in the March 18th concentration results. The SAR pixel locations are accurate to within 3.5 nm in longitude and 6.2 nm latitude which is much less than the 1 degree error needed to account for the concentration differences. A digital analysis of coarse resolution SAR imagery produced a multiyear ice concentration estimate of 52.8% (and 53.4% using a nearest neighbor operation to remove isolated pixels) corresponding to 53.0% from a manual interpretation of the same area verifying the accuracy of the manual SAR estimates.

6.0 REFERENCES

1. Hollinger J., "DMSP Special Sensor Microwave/Imager Calibration/Validation," DMSP Final Report Vol. 1, Space Sensing Branch of the Naval Research Laboratory, Washington, D.C., July 1989.

2. Burns, B. A., D. J. Cavalieri, M. R. Keller, W. J. Campbell, T. C. Grenfell, G. A. Maykut, and P. Gloersen, "Multisensor Comparison of Ice Concentration Estimates in the Marginal Ice Zone," Journal of Geophysical Research, Vol. 92, No. C7, June 1987, pp. 6843-6856.

3. Burns, B. A., R. R. Jentz, C. G. Caruthers, J. D. Lyden, and P. L. Jackson, "Computer-Assisted Techniques for Geophysical Analysis of SAR Sea-Ice Imagery," Proceedings of the Nineteenth International Symposium on Remote Sensing of Environment, Environmental Research Institute of Michigan, Ann Arbor, Mich., 1985, pp. 947-959.

4. Martin, S., B. Holt, D. J. Cavalieri, and V. Squire, "Shuttle Imaging Radar B (SIR B) Weddell Sea Ice Observations: A Comparison of SIR-B and Scanning Multichannel Microwave Radiometer Ice Concentrations," Journal of Geophysical Research, Vol.92, No. C7, June 1987, pp. 7173-7179.

5. Cavalieri, D. J., P. Gloersen, and W. J. Campbell, "Determination of Sea Ice Parameters with the Nimbus 7 SMMR," Journal of Geophysical Research, Vol. 89, 1984, pp. 5355-5369.

6. Gloersen, P. J., and D. J. Cavalieri, "Reduction of Weather Effects in the Calculation of Sea Ice Concentration from Microwave Radiance," Journal of Geophysical Research, Vol. 91, 1986, pp. 3913-3919.

7. Swift, C. T., and D. J. Cavalieri, "Passive Microwave Remote Sensing for Sea Ice Research," EOS Trans., AGU, Vol. 66, 1985, pp. 1210-1212.

8. Hollinger, J., R. Lo, G. Poe, R. Savage, and J. Peirce, "Special Sensor Microwave User's Guide," Naval Research Laboratory, Washington, D.C., September 1987.

9. Gineris, D., R. Shuchman, J. Lyden, A. Milman, E. Kasischke, "Alaska Collection SAR Data Summary," Environmental Research Institute of Michigan Report No. 202800-1-T, Ann Arbor Mich., January 1989.

10. Swift, C. T., and D. J. Cavalieri, "Passive Microwave Remote Sensing for Sea Ice Research," EOS Trans, American Geophysical Union, Vol. 66, No. 49, December 1985.

11. Gray, A. L., "Microwave Remote Sensing of Sea Ice," Oceanography From Space, 1981, pp. 785-800.

6.0 REFERENCES (cont.)

12. Onstott, R. G., T.C. Grenfell, C. Matzler, C.A. Luther, and E.A. Svendsen, "Evolution of Microwave Sea Ice Signatures During Early Summer and Midsummer in the Marginal Ice Zone," J. Geophys. Res., Vol.92, No. C7, 1987, pp. 6825-6835.

13. Gray, A. L., R. K. Hawkins, E. E. Livingstone, L. D. Arsenault, and W. M. Johnstone, "Simultaneous Scatterometer and Radiometer Measurements of Sea-Ice Microwave Signatures," IEEE J. Oceanic Eng., Vol. OE-7, 1982, pp. 20-32.

14. Mardia, K.V., J.T. Kent, J.M. Bibby, Multivariate Analysis, Academic Press, 1979.

15. Lachenbruch, P.A. Discriminant Analysis, Hafner Press, 1975.

16. Haralick, R.M., K. Shanmugam, I. Dinstein, "Textural Features for Image Classification," IEEE Trans. Syst., Man, Cybern., Vol. SMC-3, pp.610-621, 1973.

APPENDIX: EFFECTS OF PRESSURE RIDGES ON SSM/I VALUES

Results from the intercomparison of the ice concentrations produced using SAR and SSM/I data show that for an area of 100% first-year ice (based on high-resolution SAR images) with no open water or multiyear ice, that the SSM/I derived ice fraction estimates for multiyear were 30%. Similar disagreements were also found in regions of multiyear and first-year ice mixtures. The discussion provided here outlines the possible mechanisms that may be responsible. The characteristic that stands out for the multiyear free region is that the area is not composed solely of homogenous first-year ice, but includes numerous pressure ridges. Estimates based on these SAR data show that the areal coverage by the ridges for three non-adjacent regions ranged from 12.5% to 13.9%. It is known from high-resolution active-microwave observations that pressure ridges produce an enhanced backscatter due to tilted ice blocks (slope tilted normal to the radar viewing direction) and to multiple bounce scattering (i.e., dihedral etc.). However, it has been argued that passive microwave observations are impacted little by surface roughness variation since roughness is a second-order contributor in the radiative transfer formulations for emission. The results obtained in this study suggest that the impact of pressure ridges on the ice landscape is more complex than that strictly of a roughness feature. Physically, pressure ridges represent an important perturbation to the surrounding sea ice area, which, based on the data observed in this study, significantly impacts the brightness temperature signature for the ice field. Effects associated with pressure ridges may be characterized as follows: (1) features with a distribution of titled surfaces which impact the brightness temperature because of variations in the local slopes of the dielectric slabs (i.e., ice blocks), (2) "snow-fences" which allows snow accumulations up to 1 meter or more on or about the ridge, (3) enhanced brine concentration at the

base of ridges due to the mass associated with a ridge and the depression of the flat ice about a ridge with probable flooding of the ice surface with sea water, (4) scattering loss enhancement due to drainage of brine from the ice blocks above freeboard making the ice potentially less lossy and susceptible to scattering losses associated with the potential increase in porosity due to brine drainage and internal heating due to solar radiation effects, (5) induction of losses due to multiple scatterings that occur because of the rattling around within the pressure ridge with a structure that includes voids the sizes of the block that go into the construction of the ridge, and (6) multiple facet scattering losses which result from the titled block surfaces.

All of the above effects may work to produce scattering losses which result in a reduction in the brightness temperature for first-year ice. This reduction has two effects. It appears that a one degree change in brightness temperature may produce about a 2 percentage point change in ice fraction. Increased scattering losses makes first-year ice have a signature which fall between that of smooth first-year and multiyear ice.

Measurements obtained for the DC-8 37 GHz radiometer operated at V-polarization are summarized in Table A-1. These data also show two first-year ice categories with the difference related to roughness. These two clusters observed in Figure A-1 are for smooth first-year (T_B = 254 K) and rough first-year (T_B - 232 K). There is a 22 K difference between them. Hence, the significance of the rough first-year ice signature is that it's brightness temperature is 47% of the way to that of multiyear ice.

In summary, rough first-year ice has a microwave signature (both active and passive) which is dissimilar to that of smooth first-year ice. This difference is shown to impact the estimate of ice fraction for SSM/I. There are a number of contributors which have been

identified which are associated with pressure-ridge features and may be responsible for the changes in the first-year ice signature due to pressure ridge features.

TABLE A-1.

BRIGHTNESS TEMPERATURE VALUES FOR SEA ICE COLLECTED DURING THE MARCH 1988 DC-8 DATA COLLECTION

ICE TYPE	BRIGHTNESS TEMPERATURE MEAN -K-	BRIGHTNESS TEMPERATURES RANGE -K-
Multiyear	207	109 to 220
Rough First-Year	232	220 to 246
Smooth First-Year	254	243 to 258
Young First-Year	259	259 to 261

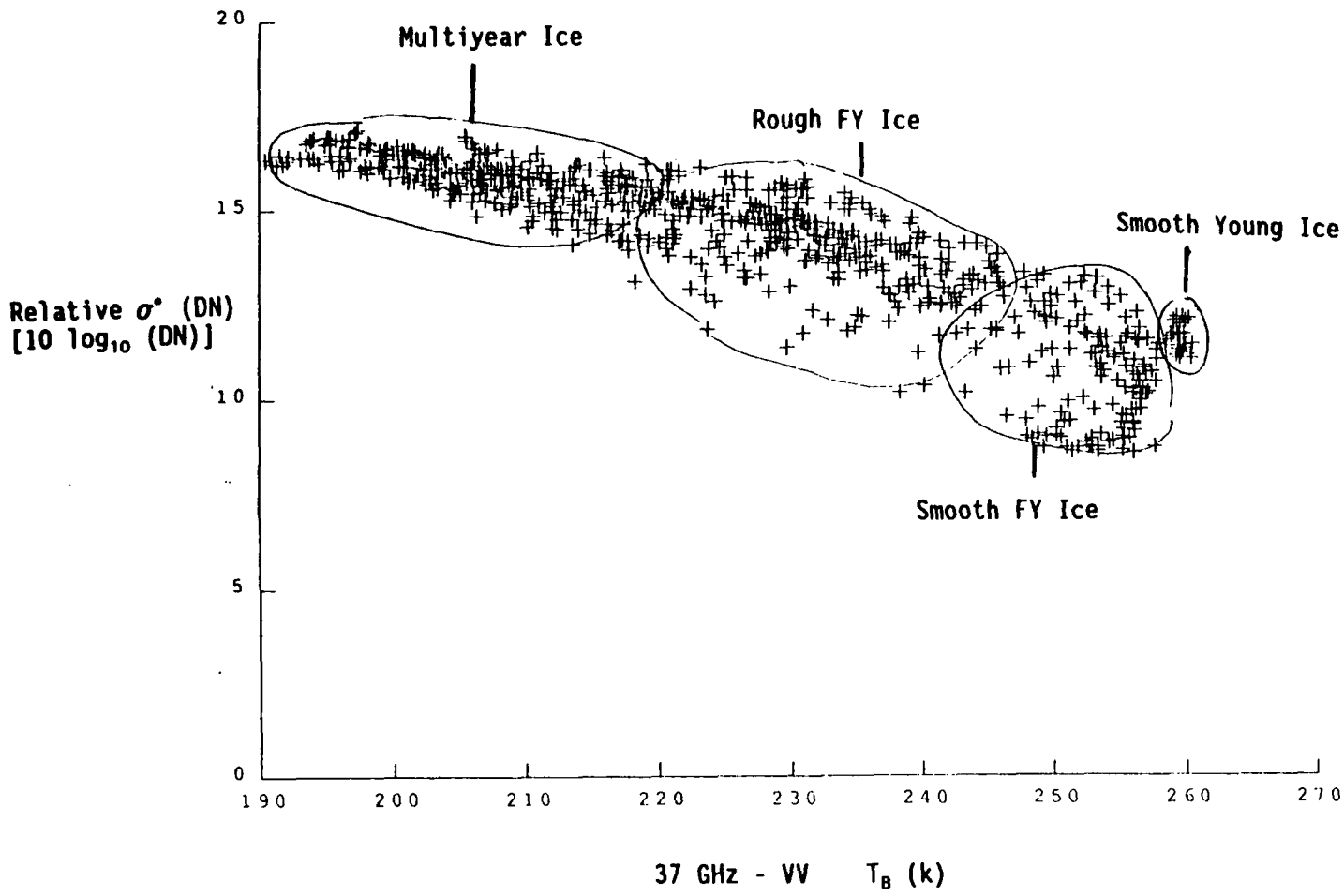

Figure A-1. Brightness Temperature and Normalized Scattering Coefficient Values for Sea Ice Collected During the March 1988 DC-8 Data Collection (From Personal Communication with Drinkwater and Crawford).

ERIM